



# Spectral Engineering Via Complex Patterns of Circular Nano-Object Miniarrays: II. Concave Patterns Tunable by Integrated Lithography Realized by Circularly Polarized Light

Emese Tóth<sup>1</sup> · Áron Sipos<sup>2</sup> · Olivér A. Fekete<sup>1</sup> · Mária Csete<sup>1</sup>

Received: 8 April 2020 / Accepted: 13 October 2020 / Published online: 13 November 2020  
© The Author(s) 2020

## Abstract

The use of circularly polarized beams in interferometric illumination of colloid sphere monolayers enables the direct fabrication of rectangular patterns composed of circular nanohole miniarrays in metal films. This paper presents a study on the spectral and near-field effects of complex rectangular patterns consisted of a central nanoring and slightly rotated satellite nanocrescents in azimuthal orientations, which promote coupling between localized and propagating plasmons. To inspect the localized modes separately, we investigate the spectral responses and near-field phenomena of hexagonal patterns composed of uniform nanorings and nanocrescents, which can be fabricated by a single, homogeneous, circularly polarized beam incident perpendicularly and obliquely, respectively. To understand the interaction of localized and propagating modes, we analyze artificial rectangular patterns composed of a singlet nanoring, a singlet horizontal nanocrescent, and a quadrumer of four slightly rotated nanocrescents. The results demonstrate that on the rectangular pattern of a singlet horizontal nanocrescent the interacting C2 and C1 localized resonances in the C orientation (0° azimuthal angle) and the U localized resonance coupled with propagating surface plasmon polaritons (SPPs) in the U orientation (90° azimuthal angle) manifest themselves in similar split spectra. Moreover, split spectra appear due to the coupling of the azimuthal orientation independent localized resonance on the nanorings and the SPPs propagating on their rectangular pattern in the U orientation. The spectral response of the complex miniarray pattern can be precisely tuned by varying the geometrical parameters of the moderately interacting nanoholes and the pattern period. In appropriate configurations, the fluorescence of the dipolar emitters is enhanced, which has potential applications in bio-object detection.

**Keywords** Concave nano-object patterns · Fluorescence enhancement of dipolar emitters · Localized surface plasmon resonance · Nanoplasmonics · Spectral engineering · Surface plasmon polariton · Tunable near-field properties · Tunable spectral properties · Wood–Rayleigh anomaly

## Introduction

Surface plasmons were rediscovered through the recognition of unique spectral and near-field properties of hole arrays in metal films [1–5]. Such concave patterns can act as

plasmonic crystals, and the resulting optical properties can be tuned by controlling the shape and size parameters of either the constituent nanoholes or the periodic pattern. Depending on the size, shape, and relative orientation with respect to the direction of the electric field ( $\vec{E}$ -field) oscillation, an individual nanohole in a metal film can spectrally modulate and significantly enhance the  $\vec{E}$ -field [2, 4, 5]. Among the different possible geometries, C-shaped apertures are particularly interesting because they can result in an  $\vec{E}$ -field enhancement by three orders of magnitude and a confinement down to a tenth of the wavelength, as first demonstrated in the microwave region [4, 6]. Extraordinary transmission can occur through arrays of sub-wavelength holes of various shapes [1–5]. The earliest studies of this phenomenon revealed that transmittance minima (maxima)

---

✉ Mária Csete  
mcsete@physx.u-szeged.hu  
Áron Sipos  
sipos.aron@brc.hu

<sup>1</sup> Department of Optics and Quantum Electronics, University of Szeged, Szeged H-6720, Hungary

<sup>2</sup> Institute of Biophysics, Biological Research Centre, Szeged H-6726, Hungary

appear at the spectral positions corresponding to the Rayleigh (resonant Wood) anomaly, which is related to the photonic mode scattering at a grazing angle (to a propagating surface plasmon polariton (SPP) excitation) [7, 8]. An important difference with respect to photonic crystals is that SPPs propagate in the plane of topographic modulation on hole arrays in metal films, which act as lossy plasmonic crystals. Previous works showed that nanoholes cause band bending and the appearance of bandgaps, which indicates that the application of a simple planar interface approximation to explain the dispersion branches can cause discrepancies [9, 10]. At the bandgaps, standing SPP waves were detected on rectangular arrays of sub-wavelength holes via scanning near-field optical microscopy [11]. The main design rules of plasmonic spectral engineering rely on the interplay between the Fabry Perot resonances localized inside individual nanoholes, resulting in broad spectral lines, and grating-coupled resonances on plasmonic lattices, resulting in narrow spectral lines [3–5]. In two-dimensional hole arrays, the periodicity in a certain direction is described by a lattice vector  $\vec{k}$ , and when the  $\vec{E}$ -field projection is significant along  $\vec{k}$ , the parallelism promotes coupling between SPPs and the grating. In other words, narrow spectral features originating from higher-order Bragg resonances were identified on microscale rectangular arrays of nanoholes [12]. Furthermore, the interaction of coupled localized surface plasmon resonances (LSPRs) and SPPs was demonstrated to result in a complex and finely tunable spectral response [13]. Concave patterns in metal films have already various important applications. Coupled resonances resulting in narrow Fano-lines are particularly beneficial in biosensing applications [14]. The polarization insensitivity of square arrays of spherical nanoholes enables the polarization entanglement to be preserved [15]. Moreover, elliptical holes arranged in pairs of sub-lattices enable polarization-induced frequency shifts [16]. The first metamaterials to achieve spectral effect close to the visible region were created by using rectangular arrays of sub-wavelength holes [17]. For example, C-shaped apertures were used to enhance the photocurrent in Ge detectors at 1310 nm, with maximum efficiency obtained with the  $\vec{E}$ -field direction parallel to the arms of the aperture [18]. Several examples prove that the widely tunable grating-coupled resonances, when using nanovoid and nanohole arrays, enable high sensitivity biosensing [19]. Combined spectral and near-field studies revealed that the transmittance minima (maxima) exhibit smaller (larger) sensitivity on hexagonal and square hole arrays [20–22]. Moreover, special individual scatterers such as hole doublets ensure enhanced sensitivity due to the antennas that appear at their apexes [4, 23]. In addition, transmittance peaks corresponding to Bragg resonances along the  $\vec{E}$ -field direction produce considerably enhanced sensitivity for square arrays [24]. The high local-field

enhancement obtained by using nanorings embedded into a continuous metal film can be applied in surface-enhanced Raman spectroscopy [25]. Nano-apertures in metal films also enhance the fluorescence efficiency, which facilitates single-molecule detection [26, 27]. The common advantage of structures with rectangular unit cells is that typically smaller size enables them to be efficient in the near-infrared, which is especially important for biodetection [28]. The strong-coupling regime of photochromic molecules can be reached by using a hole array platform [29]. Steady-state superradiance can be achieved by coupling SPPs on a two-dimensional hole array via dye molecules arranged above the holes [30]. Moreover, lasing in a semiconductor gain medium governed by metal hole array dispersion was also demonstrated [31, 32]. Complementary C-shaped split-ring resonators were proposed to design metasurfaces with potential applications as frequency- and polarization-selective filters [33]. Directional coupling of SPPs was achieved by arrays of complementary C-shaped split-ring resonators, which facilitates the miniaturization of photonic and plasmonic circuits [34]. Babinet inverted plasmonic metasurfaces were used to produce spin-selective second-harmonic vortex beams [35]. It was shown that disks and cylindrical apertures differ quantitatively with respect to the Babinet complementarity because the apertures produce higher magnetic-to-electric-field ratios and better charge-transfer properties [36]. Miniarrays of elliptical nanoholes that are not superimposable on their mirror image exhibit chiroptical effects, i.e., selective reflection of a single spin state while preserving its handedness [37]. However, fabrication of non-hexagonal (e.g., rectangular) arrays of nano-objects was previously possible only by expensive and complex electron-beam lithography procedures [38]. Double-exposure, two-beam interference lithography has been applied to fabricate one-dimensional and two-dimensional structures in gold film (e.g., rectangular array of nanoholes) [39]. Colloid sphere lithography has been used to generate imprinted nanochannel alumina patterns with hexagonal symmetry [40]. Laser-based colloid sphere lithography can be used to fabricate nanoholes via colloid spheres, which can be isolated, aggregated and embedded into monolayers, and the parameters of the fabricated nanoholes depend on the size and material of the colloid spheres, on the environment and laser parameters [41]. Tilting during treatment makes it possible to fabricate sub-diffraction objects of arbitrary shape [42]. As an alternative method, the combination of phase-shifting lithography, etching, electron-beam deposition, and lift-off procedure was developed and used to fabricate microscale periodic rectangular arrays of nanoscale holes [12]. Nanorings have been also prepared by biomolecule-assisted deposition of gold spheres into previously fabricated nanoholes [25]. To overcome the limitations of laser-based colloid sphere lithography, chemical treatments were applied to create Janus and

patchy colloids, template-based substrates were fabricated to ensure geometrical confinement, and electric as well as magnetic forces were applied to position colloid assemblies [43]. Multiscale periodic colloid assemblies were created by combining thermo-responsive depletion with pre-patterned surface features [44]. In our previous studies, we presented the interferometric illumination of colloid sphere monolayers (IICSM) that enables the independent tuning of numerous geometrical parameters [45, 46]. The method combines colloid sphere (CS) and interference lithography and synthesizes all the advantages of these methods, thus providing a good tool to fabricate versatile patterns. In our previous papers, we presented the IICSM method for illumination by linearly [45] and circularly [46] polarized light. In this paper, we present and discuss the spectral and near-field effects achievable by complex patterns of rounded nanoholes; more precisely, by miniarrays of nanorings and nanocrescents that form an ordered and pre-designed rectangular pattern. The rounded objects originate from illumination using circularly polarized beams and form miniarrays defined by the specific interferometric illumination configuration. For reference purposes, we also discuss spectral and near-field effects achievable by hexagonal patterns of nanorings and nanocrescents that originate from the illumination of CS monolayers by a single, homogeneous perpendicularly and obliquely incident circularly polarized beam, respectively. The spectral and near-field effects of the building blocks arranged in rectangular patterns (i.e., a singlet nanoring, a singlet horizontal nanocrescent, and a quadrumer of slightly rotated satellite nanocrescents) are also analyzed. The potential of all these structures to enhance the fluorescence of dipolar emitters is also demonstrated. Part I of this paper describes the spectral and near-field effects of the analogous convex patterns [47]. Reference [46] presents a comparative study on the spectral and near-field effects of complementary concave and convex patterns, which can be directly fabricated via IICSM followed by a lift-off procedure. Finally, a detailed comparative study on the corresponding optical responses of complementary patterns [i.e., the reflectance (transmittance) of the concave patterns and the transmittance (reflectance) of the convex patterns] will be presented in our upcoming paper [48].

## Method

### Numerical Modeling and Characterization of Patterns Composed of Concave Spherical Nano-Objects

We used the radio frequency finite-element method (FEM) module of COMSOL Multiphysics software package (COMSOL AB, Sweden) to study the structures that can be fabricated by illumination using a single homogeneous

circularly polarized beam and by IICSM using two circularly polarized beams. In this study,  $d = 100$ -nm-diameter gold colloid spheres are arranged into a hexagonally close-packed monolayer on a 45-nm-thick gold-coated NBK7 substrate and are illuminated by a single homogeneous, perpendicularly or obliquely incident beam or by two obliquely incident interfering beams, which are  $\lambda = 400$  nm and circularly polarized. The illumination of one unit cell of hexagonal gold CS monolayer was realized by using three-dimensional periodic models, which enabled the use of any desired azimuthal orientation and angle of incidence for a single beam as well as for multiple beams. All materials were modeled by taking into account the wavelength-dependent optical properties. More specifically, the NBK7 glass was qualified by using the Cauchy formula  $n = A + \frac{B}{\lambda^2} + \frac{C}{\lambda^4}$  ( $A_{NBK7} = 1.503$ ,  $B_{NBK7} = 4.395 \cdot 10^3$ ,  $C_{NBK7} = 8.585 \cdot 10^5$ ) [49], whereas, for gold, tabulated data sets were interpolated to implement the wavelength-dependent dielectric properties [50]. The schematic drawing in Fig. 1a shows the IICSM concept for illumination by two circularly polarized beams. The required condition for the IICSM method is the perfect synchronization of a hexagonal close-packed CS monolayer and an illuminating interference pattern. Figure 1b and 1c shows the main characteristic geometrical parameters that can be varied via IICSM with a circularly polarized beam. In the so-called close-packed in-between array configuration, the  $p^n$  periodicity can be tuned to  $p^n = n \cdot d/2$  discrete values, which are achievable at the angle of incidence  $\theta^n = \arcsin(\lambda/(n \cdot d))$ , where  $d$  is the CSs diameter, and  $n \geq 1$  is an integer. The angle  $\alpha$  identifies the orientation of the plane of incidence with respect to the (100) lattice direction of the hexagonal monolayer, and the resulting inter-object distance  $t$  varies with the corresponding orientation  $\beta$  of the interference pattern. Figure 1b and 1c shows the complex interference pattern, and the resulting concave pattern in a gold layer, which is inspected in this work, where  $t = \sqrt{3} \cdot d$  is the inter-object distance fabricated for  $\beta = 30^\circ$ . The parameters  $d_0$  and  $d'$  determine the nano-object size and are tunable by adjusting the wavelength  $\lambda$  and the beam intensity, as well as by adjusting the CSs diameter  $d'$  and its material. In the present study,  $d = d' = 100$  nm, which implies the assumption that the gold colloid spheres touch each other. This assumption is reasonable, since our previous studies showed that the nano-object parameters are not significantly modified when the diameter is reduced ( $d' < d$  condition ensures a greater intensity at the substrate interface than at the monolayer central plane where the spheres touch each other). Both the nanoring and nanocrescent stem from the circular polarization of the beams, proving that the exact shape of the generated nanoholes is polarization dependent [45, 46].

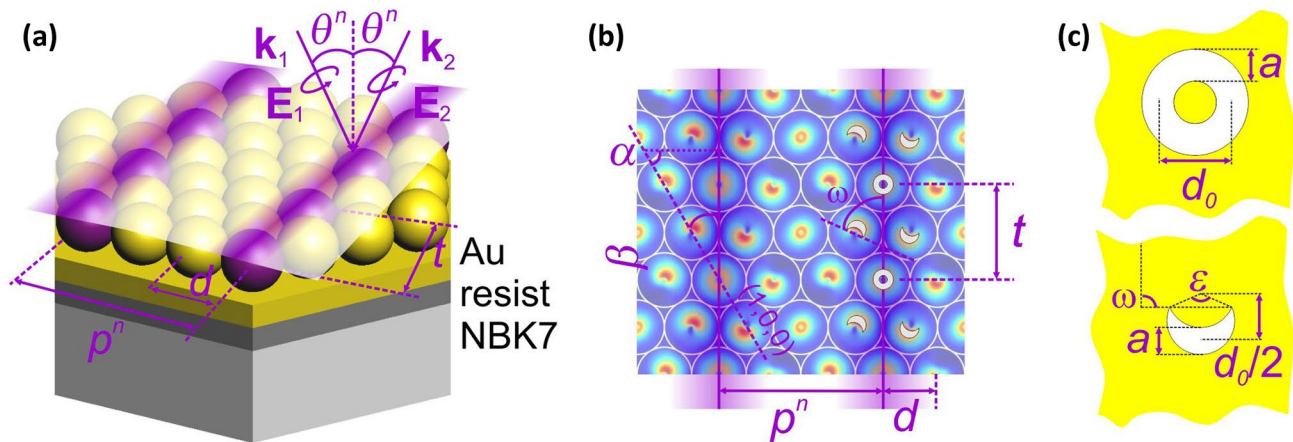


**Fig. 1** Schematic drawings showing characteristic size parameters: (a) three-dimensional scheme of periodic pattern fabrication by interferometric illumination of  $d$  diameter CS, where  $\theta^n$  polar angle defines the  $p^n$  pattern period (b)  $\alpha$  orientation of the plane of inci-

dence defines the  $\beta$  orientation of the resulting interference pattern, which is used to tune the distance  $t$  between nano-objects, (c) generated features qualified by the central diameter  $d_0$ , the central thickness  $a$ , the opening angle  $\epsilon$ , and the nano-object orientation  $\omega$

### Spectral and Near-Field Study of Various Patterns

The complete spectral study of 45-nm-thick gold films decorated by different nanohole patterns was realized, i.e., the effect of these complex patterns on the optical response and on the near-field distribution was determined. Floquet periodic boundary conditions were applied on vertical boundaries of the FEM (COMSOL) models, which composed of various hexagonal and rectangular unit cells exposed to p-polarized plane-wave post-illumination. The inspected realistic hexagonal patterns are as follows: a hexagonal pattern of (i) nanoring-shaped holes (Figs. 2a, 3a, 3b, 3d), and (ii) horizontal nanocrescent-shaped holes (Figs. 2b, 3, 3c, 3e; vertical nanocrescents are presented in the Supplementary Material). The nanoholes are called nanorings and nanocrescents for the sake of simplicity. The studied artificial composing rectangular patterns are as follows: a 300 nm rectangular pattern of (iii) a singlet nanoring (Fig. 4), (iv) a singlet horizontal nanocrescent (Fig. 5), and (v) a quadrumer of slightly rotated nanocrescents (Fig. 6). Finally, two different rectangular patterns were analyzed: a (vi) 300 nm (Figs. 2c, 7) and (vii) 600 nm periodic (Figs. 2d, 8) rectangular pattern of the same miniarray consisted of a central nanoring and a quadrumer of slightly rotated nanocrescents. In this spectral study, p-polarized light with incidence plane oriented at  $\gamma$  azimuthal angle (that is measured with respect to the y axis in the insets of Figs 3–8) illuminated the perforated gold film in a symmetric environment, meaning that the film was surrounded by NBK7 glass and the nanoholes were filled with the same material. To uncover the characteristic LSPRs supported by the nanoholes without grating-coupling to either the photonic or plasmonic modes, the hexagonal pattern of concave nanorings and nanocrescents were inspected in  $0^\circ$

and  $90^\circ$  azimuthal orientations. For rectangular patterns, both the  $90^\circ$  ( $106^\circ$ ) and  $0^\circ$  ( $16^\circ$ ) azimuthal orientations were inspected, since these promote LSPR as well as grating-coupling effects in the case of horizontal nanocrescents (LSPR in the case of the quadrumers and miniarrays). Following the nomenclature introduced for convex nanocrescents and taking into account the complementarity according to the Babinet principle, the LSPR of nanocrescent-shaped holes is called the C (U) resonance when the  $\vec{E}$ -field oscillates parallel (perpendicular) to their symmetry axis [33, 35, 36, 51]. Accordingly, in (close to) the C and U orientation refers to the illumination configuration, when the incidence plane of p-polarized light is at  $0^\circ$  ( $16^\circ$ ) and  $90^\circ$  ( $106^\circ$ ) azimuthal angle, and the  $\vec{E}$ -field oscillates perfectly (almost) parallel and perpendicular to the symmetry axis of horizontal singlet concave nanocrescents in Figs. 3 and 5. Similarly, in (close to) the C and U orientation refers to the illumination configuration, when the incidence plane of p-polarized light is at  $16^\circ$  ( $0^\circ$ ) and  $106^\circ$  ( $90^\circ$ ) azimuthal angle and the  $\vec{E}$ -field oscillates perfectly (almost) parallel and perpendicular to the symmetry axis of slightly rotated nanocrescents in quadrumers and miniarrays in Figs 6–8. Further details are provided in Refs. [46–48]. The spectra were taken over the range 200–1000 nm with 10 nm resolution and at  $\varphi = 0^\circ$  polar angle (i.e., at perpendicular incidence; see Figs. 3–8a). FEM (COMSOL) was used to inspect the dispersion characteristics of the concave patterns by selecting fractions on the high-symmetry path throughout their irreducible Brillouin zone according to the azimuthal orientations that facilitate detection of the LSPR on composing circular nano-objects and mapping of the coupled SPP branches. Accordingly, the dispersion characteristics were analyzed for the  $0^\circ$  and  $90^\circ$  azimuthal orientations. To compute the dispersion diagram, the spectral range was



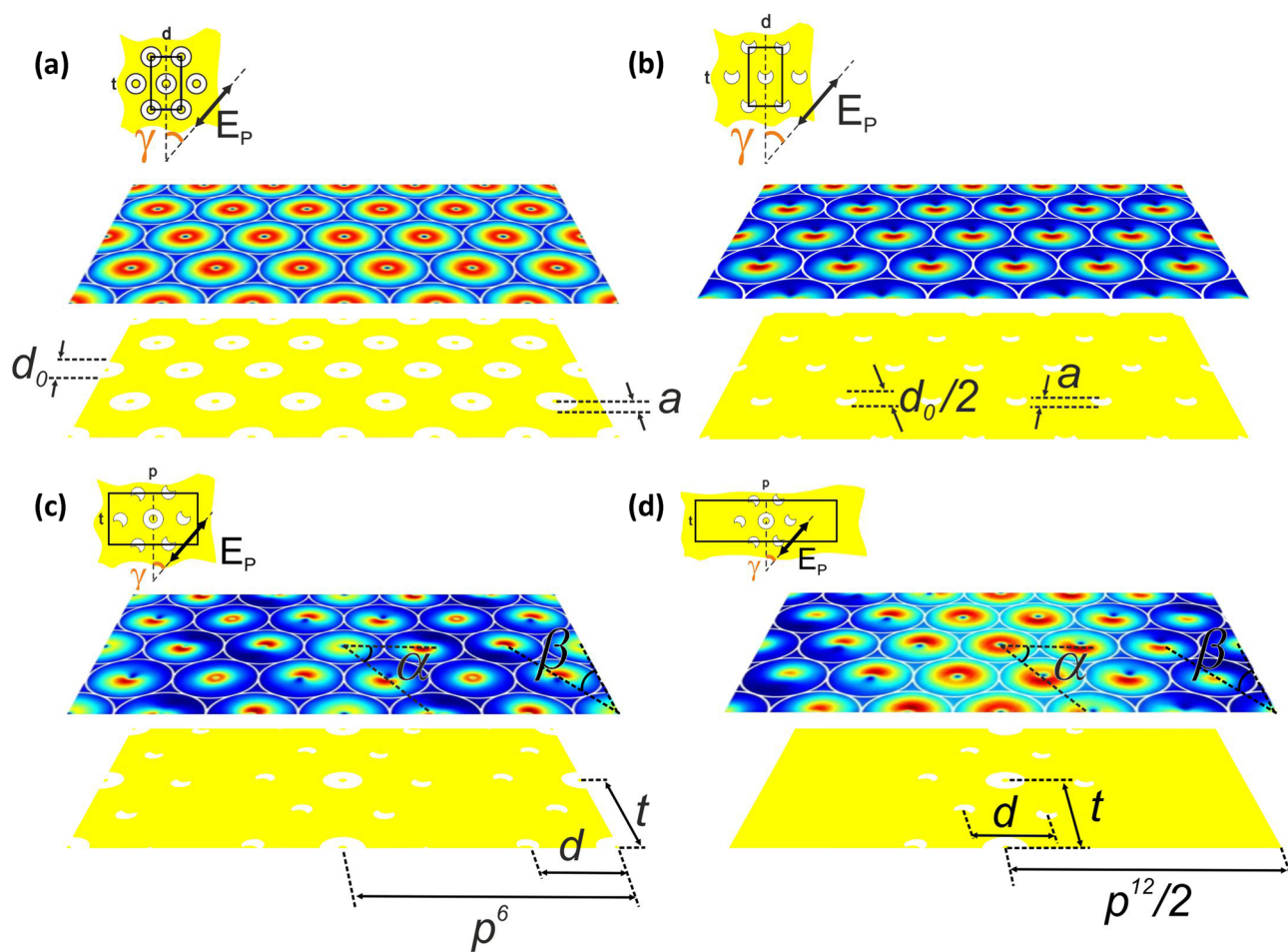


**Fig. 2** Normalized  $\bar{E}$ -field distribution under gold CS monolayers illuminated by single circularly polarized beam incident (a) perpendicularly and (b) obliquely, which results in a hexagonal pattern of nanoholes, and (c), (d) by two interfering beams (in  $\beta = 30^\circ$  orientation with respect to the (100) plane of the original CS monolayer) in

IICSM configuration, which results in a rectangular pattern of miniarrays. The insets show the unit cells of the complex patterns: a hexagonal pattern of (a) nanorings and (b) nanocrescents, and a rectangular pattern of miniarrays consisted of a central nanoring and satellite nanocrescents with (c)  $p^6 = 300$  nm and (d)  $p^{12} = 600$  nm periodicity

extended through 1000 nm with the same 10 nm wavelength resolution, as for perpendicular incidence, whereas the  $\varphi$  angle of incidence was modified from  $0^\circ$  to  $85^\circ$  in  $5^\circ$  steps (Figs. 3d, 3e, and 4-8c). To uncover all underlying modes on the dispersion graphs, higher-resolution complementary calculations were realized in smaller steps wherever needed. According to the literature, the absorptance spectra of plasmonic patterns are very useful to find resonances, so herein the absorptance spectra and dispersion characteristics are analyzed [52]. To separate the effect of complex plasmonic structures from the background of the continuous gold film, the spectra were rectified. Specifically, first the optical signal of a solid gold film of the same thickness as the perforated film was subtracted, then the absorptance values were normalized by multiplying the spectra by the ratio of unit-cell area to nanohole area (Figs. 3-8a). The near-field distribution and charge distribution were inspected by taking into

account the complementarity of the modal profiles according to the Babinet principle [33, 35, 36]. Specifically, the complementarity of the time-averaged  $E_z$  distribution on convex patterns corresponding to the time-averaged  $B_z$  distribution on concave patterns allows us to determine the accompanying time-averaged  $E_z$  distribution and the characteristic charge distribution at the C and U resonances on patterns composed of concave nanocrescents (Figs. 3b, 3c, and 4-8b) [46–48, 51]. Localized plasmon resonances on the nanorings and nanocrescents are distinguished by using r and c in the abbreviations. First- and second-order grating-coupled SPPs are denoted "SPP1" and "SPP2", respectively. The FEM was used to inspect the capabilities of the artificial patterns to enhance fluorescence, namely the rectangular patterns of a singlet nanoring and a quadrumer of nanocrescents, as well as of the rectangular patterns of their miniarray (Fig. 9).

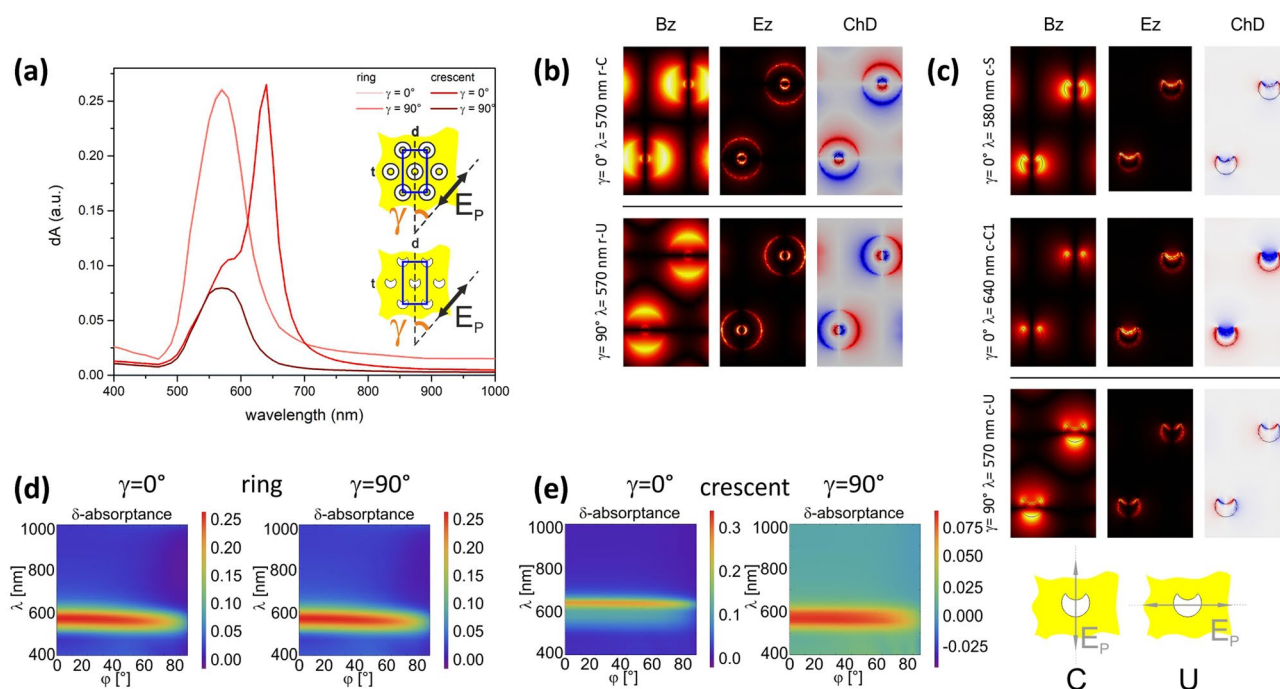


**Fig. 3** Hexagonal patterns composed of concave nanorings and horizontal nanocrescents: (a) absorbance spectra;  $B_z$  and  $E_z$  and charge (ChD) distribution in (top)  $0^\circ$  and (bottom)  $90^\circ$  azimuthal orientation of (b) nanorings and (c) nanocrescents; dispersion characteris-

tics computed for (left)  $0^\circ$  and (right)  $90^\circ$  azimuthal orientation of (d) nanorings and (e) nanocrescents. Insets show schematic drawing of the unit cells presenting the C and U configurations of horizontal concave nanocrescents

## Results and Discussion

### Patterns Achievable in Different Illumination Configurations

To determine the patterns achievable by homogeneous illumination and by IICSM, the  $\vec{E}$ -field distribution was examined at the surface of gold films. The  $d_0$  and  $a$  parameters were calculated based on the full width at half maximum of the intensity distribution. Illumination by a single, homogeneous, perpendicularly incident, circularly polarized beam results in (i) a hexagonal pattern of uniform nanorings with 10 nm and 46 nm inner and outer diameters, respectively (Fig. 2a). A single, homogeneous, obliquely incident, circularly polarized beam generates (ii) a hexagonal pattern of uniform nanocrescents; Fig. 2b shows the case for the angle of incidence  $\theta^6 = 41.8^\circ$ . The nanocrescents were approximated as the intersections of two cylindrical objects of 25 nm and 20 nm diameter separated by 12.5 nm between their centers. Figure 2c and 2d illustrates the effect of modifying the periodicity of the interference pattern in IICSM. Namely, (vi) a rectangular pattern with  $p^6 = 300$  nm periodicity appears at  $\theta^6 = 41.8^\circ$  angle of incidence, which corresponds to the case  $n = 6$ , whereas (vii) a rectangular pattern with  $p^{12} = 600$  nm develops at  $\theta^{12} = 19.5^\circ$  angle of incidence, which corresponds to the case  $n = 12$ . Taking into account

that the nano-object size parameters  $d_0$  and  $a$  are tunable by adjusting the intensity and to simplify the comparison between miniarrays with different periodicities, analogous nanohole parameters were assumed during the spectral and near-field study of both rectangular patterns, as shown in the insets of Fig. 2. Specifically, the inner and outer central nanorings have diameters of 10 nm and 50 nm, while the satellite nanocrescents have the same size parameters as in the hexagonal array (Figs. 2c and 2d).

### Spectral and Near-Field Effects of Different Patterns

The common property of the rectified absorptance extracted from concave patterns is that the fingerprints of the spectrally overlapping and interacting particle plasmon resonance (PPR) and c-C2 resonance in the C orientation, as well as the PPR signatures in the U orientation are missing. This is caused by the subtraction of the continuous film absorptance, which exhibits commensurate enhancement in the spectral interval of the PPR [47, 48]. The Babinet principle predicts that the  $E_z$  distribution on the complementary convex pattern corresponds to the  $B_z$  distribution on the concave pattern, and the accompanying  $E_z$  distribution on the concave pattern reveals the charge distribution at the characteristic resonances [33, 35, 36, 47, 48].

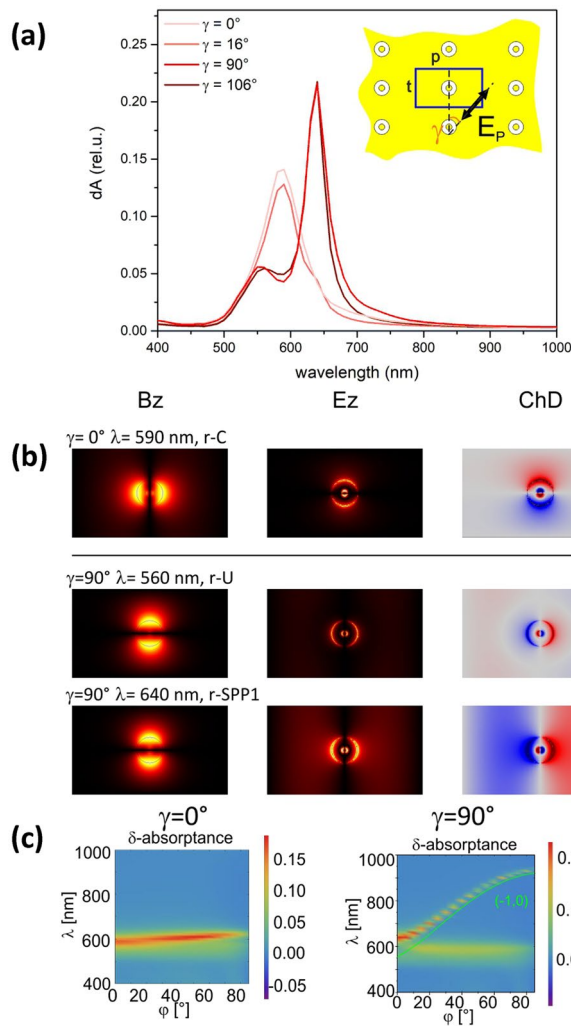


**Fig. 4** Rectangular  $p^6 = 300$  nm periodic pattern composed of a singlet concave nanoring: (a) absorbance spectra; (b)  $B_z$  and  $E_z$  and charge (ChD) distribution in (top)  $0^\circ$  and  $16^\circ$  and (bottom)  $90^\circ$  and  $106^\circ$  azimuthal orientation; (c) dispersion characteristics computed for (left)  $0^\circ$  and (right)  $90^\circ$  azimuthal orientation. Inset shows schematic drawing of the unit cell. Note that clicking on the figure switches between  $0^\circ$  and  $16^\circ$  and between  $90^\circ$  and  $106^\circ$  azimuthal orientations

**Hexagonal Pattern of Concave Nanorings**

Given the spherical symmetry of the constituent nano-objects and the symmetries of the hexagonal lattice, a single maximum appears at 570 nm in the rectified absorbance of the hexagonal pattern composed of concave nanorings azimuthal orientation independently (Fig. 3a). Moreover, the global maxima overlap completely in the  $90^\circ$  and  $0^\circ$  azimuthal orientations. The  $B_z$  distribution reveals lobes both on the inner and outer rim of the concave nanorings, perpendicular to the  $\vec{E}$ -field direction, which corresponds to the lobes of the  $E_z$  distribution on the complementary hexagonal pattern of

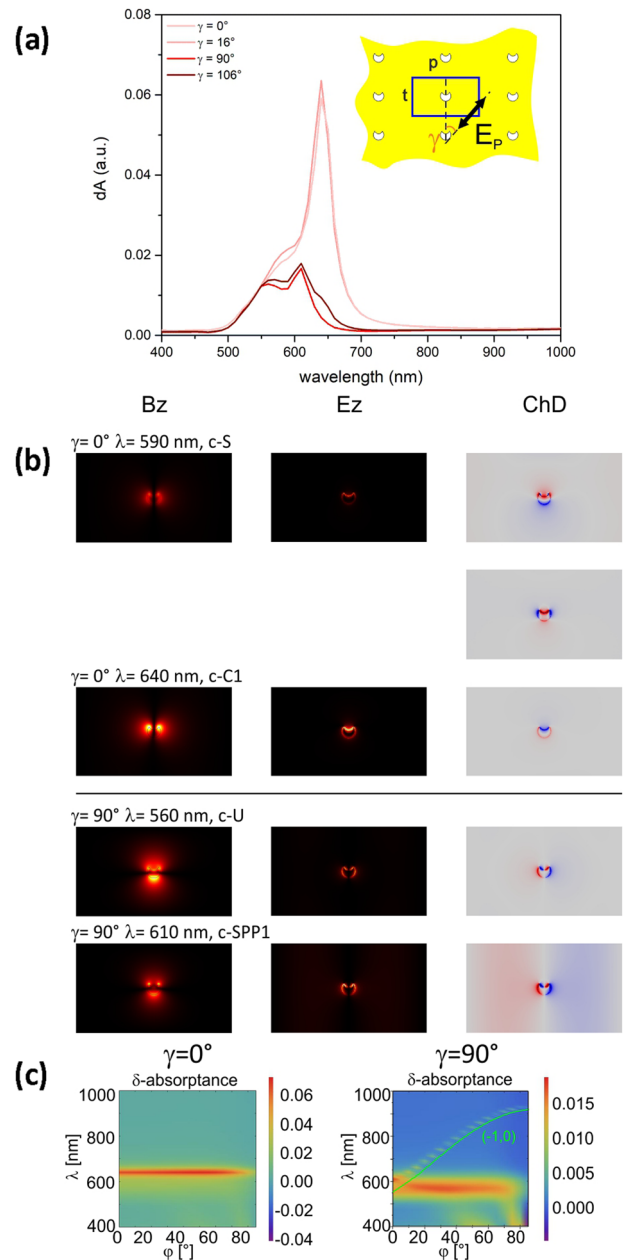


**Fig. 5** Rectangular  $p^6 = 300$  nm periodic pattern composed of a horizontal singlet concave nanocrescent: (a) absorbance spectra, (b)  $B_z$ ,  $E_z$  and charge (ChD) distribution in (top)  $0^\circ$  and  $16^\circ$  and (bottom)  $90^\circ$  and  $106^\circ$  azimuthal orientation, (c) dispersion characteristics computed for (left)  $0^\circ$  and (right)  $90^\circ$  azimuthal orientation. Inset shows schematic drawing of the unit cell. Note that clicking on the figure switches between  $0^\circ$  and  $16^\circ$  and between  $90^\circ$  and  $106^\circ$  azimuthal orientations

convex nanorings [47, 48]. In contrast, the accompanying  $E_z$  distribution indicates lobes parallel to the  $\vec{E}$ -field direction on the concave nanorings, which reveals the characteristic charge distribution composed of reversed dipoles on the inner and outer rim of the nanorings at the indistinguishable r-C and r-U resonance (Fig. 3b, top and



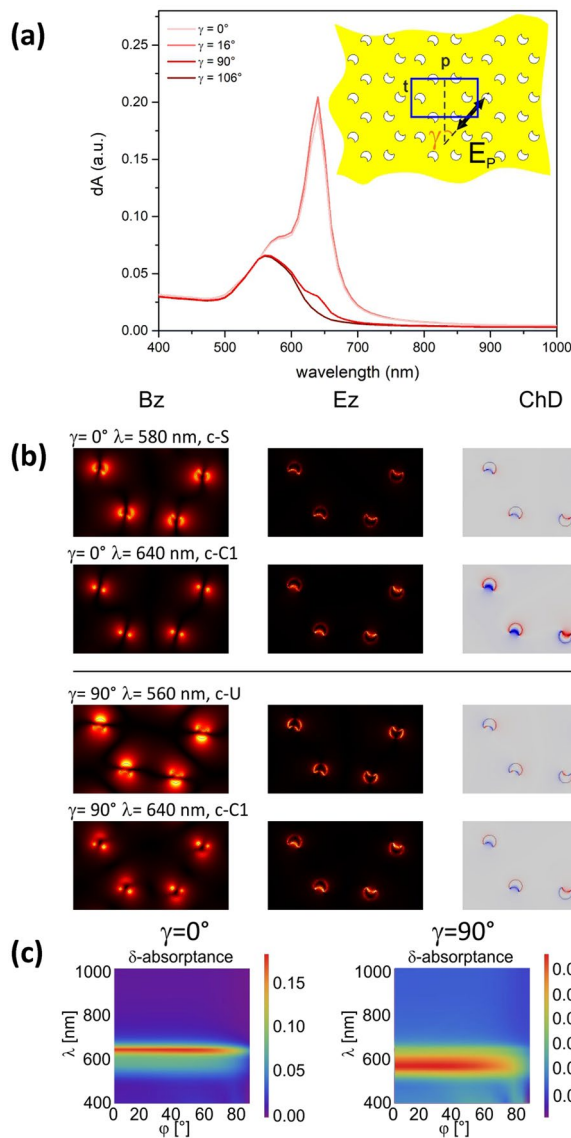


**Fig. 6** Rectangular  $p^\delta = 300$  nm periodic pattern composed of a quadrumer of concave nanorescences: (a) absorbance spectra, (b)  $B_z$ ,  $E_z$  and charge (ChD) distribution in (top)  $16^\circ$  ( $0^\circ$ ) and (bottom)  $106^\circ$  ( $90^\circ$ ) azimuthal orientation, (c) dispersion characteristics computed for (left)  $0^\circ$  and (right)  $90^\circ$  azimuthal orientation. Insets show schematic drawing of the unit cell. Note that clicking on the figure switches between  $0^\circ$  and  $16^\circ$  and between  $90^\circ$  and  $106^\circ$  azimuthal orientations

bottom). The azimuthal orientation independent r-C and r-U LSPRs on the nanoring result in a single flat band in the dispersion characteristics (Fig. 3d).

### Hexagonal Pattern of Horizontal Concave Nanorescences

**Hexagonal Pattern of Horizontal Concave Nanorescences in the C Orientation** In the rectified absorbance of the hexagonal array composed of horizontal concave nanorescences,

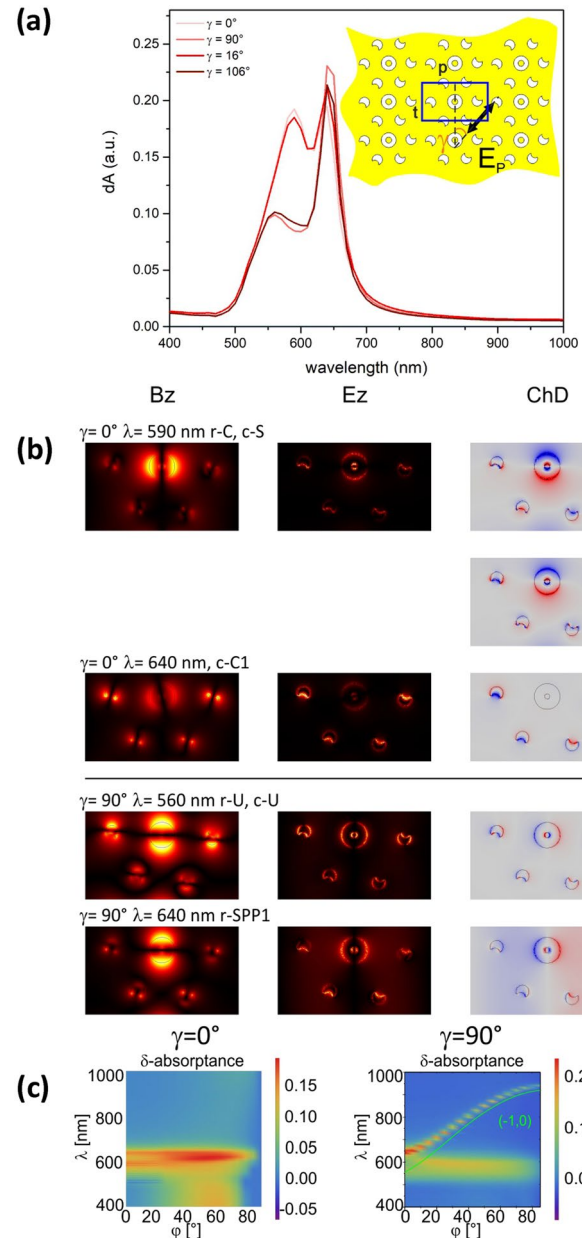


**Fig. 7** Rectangular  $p^\delta = 300$  nm periodic pattern composed of a complex concave miniarray: (a) absorbance spectra, (b)  $B_z$ ,  $E_z$ , and charge (ChD) distribution in (top)  $16^\circ$  ( $0^\circ$ ) and (bottom)  $106^\circ$  ( $90^\circ$ ) azimuthal orientation, (c) dispersion characteristics computed for  $0^\circ$  (left) and  $90^\circ$  (right) azimuthal orientation. Inset shows a schematic drawing of the unit cell. Note that clicking on the figure switches between  $0^\circ$  and  $16^\circ$  and between  $90^\circ$  and  $106^\circ$  azimuthal orientations

a shoulder at 580 nm is followed by a global maximum at 640 nm in the C orientation ( $0^\circ$  azimuthal angle) (Fig. 3a). On the  $B_z$  distribution, the four neighboring c-C2 resonance-related and the two c-C1 resonance-related lobes result in two well-separated composite lobes at the shoulder. This is accompanied by three bright and three weak lobes on the  $E_z$  distribution on the small and large arch of the nanorescences,



**Fig. 8** Rectangular  $p^{12} = 600$  nm periodic pattern composed of a complex concave miniarray: (a) absorptance spectra, (b)  $B_z$ ,  $E_z$ , and charge (ChD) distribution in (top)  $16^\circ$  ( $0^\circ$ ) and (bottom)  $106^\circ$  ( $90^\circ$ ) azimuthal orientation, (c) dispersion characteristics computed for  $0^\circ$  (left) and  $90^\circ$  (right) azimuthal orientation. The insets show schematic drawings of the unit cell. Note that clicking on the figure switches between  $0^\circ$  and  $16^\circ$  as well as between  $90^\circ$  and  $106^\circ$  azimuthal orientations

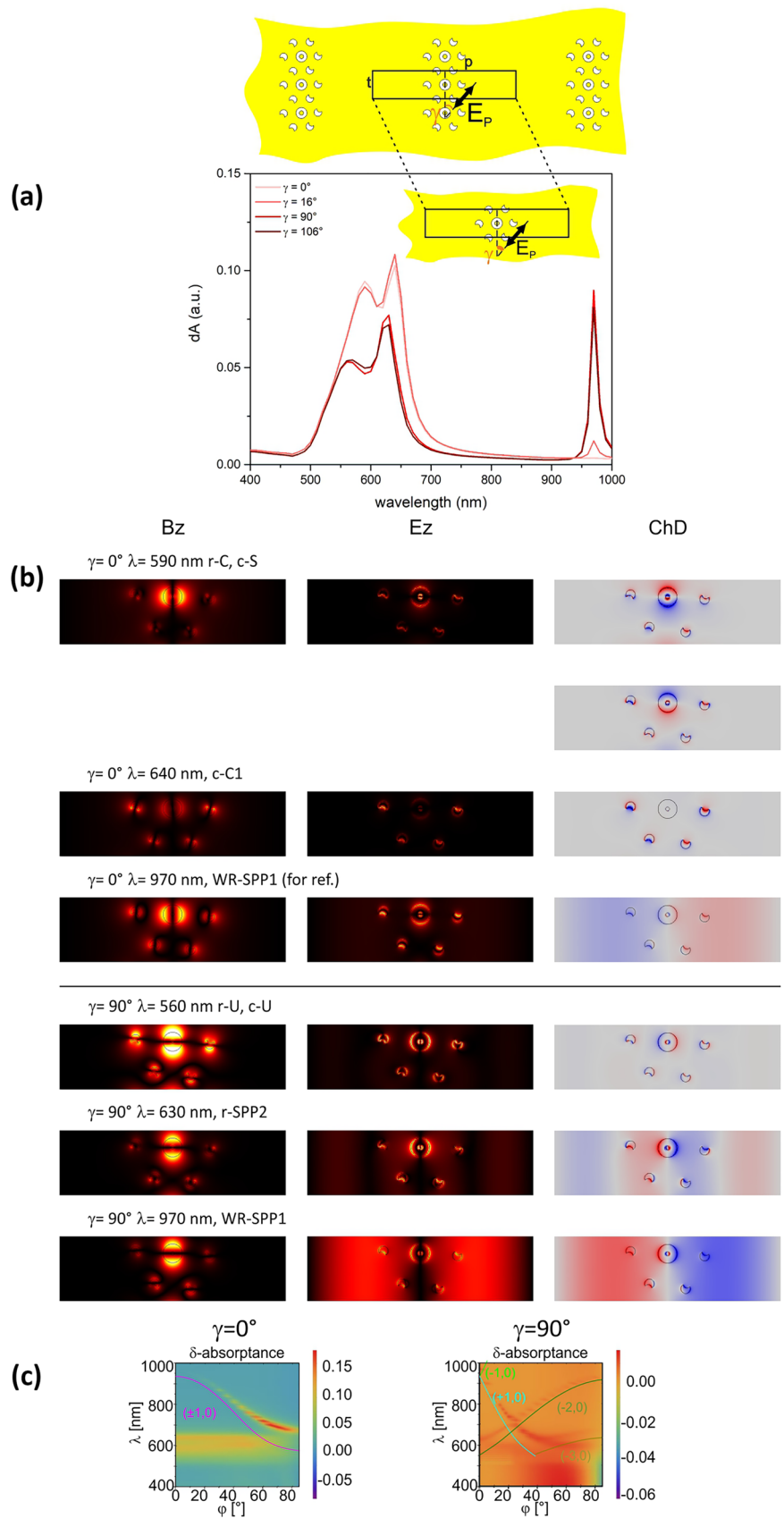
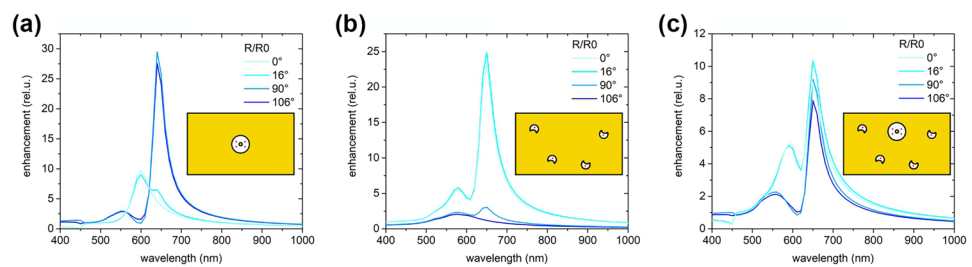


**Fig. 9** Radiative rate enhancement spectra of dipolar emitters achievable via 300 nm rectangular patterns composed of (a) a singlet nanoring, (b) a quadrumer of nanocrescents, (c) a complex miniarray



respectively. Accordingly, the characteristic charge distribution is hexapolar. At the global maximum, the two nanocrescent tips are coincident with the maxima on the  $B_z$  distribution; this is accompanied by two lobes of the  $E_z$  distribution on the arches of the nanocrescents, with the significantly stronger lobe on the smaller arch. The characteristic charge distribution is dipolar along the  $\vec{E}$ -field direction at the c-C1 resonance (Fig. 3c, top). The interacting c-C2 and c-C1 LSPRs on the horizontal nanocrescent result in two overlapping flat bands in the dispersion characteristics (Fig. 3e, left).

**Hexagonal Pattern of Horizontal Concave Nanocrescents in the U Orientation** In comparison, in the rectified absorbance of the hexagonal pattern composed of horizontal concave nanocrescents, only the global maximum appears (at 570 nm) in the U orientation ( $90^\circ$  azimuthal angle) (Fig. 3a). Two  $B_z$  lobes appear at the global maximum: one on the large arch and the other distributed on the tips, which is accompanied by four lobes on the  $E_z$  distribution on the nanocrescents. The characteristic charge distribution is quadrupolar and governed by the  $\vec{E}$ -field direction at the c-U resonance (Fig. 3c, bottom). The c-U LSPR on the horizontal nanocrescent results in a single wide band in the dispersion characteristics (Fig. 3e, right).

#### Rectangular 300 nm Periodic Pattern of a Singlet Concave Nanoring

**Rectangular 300 nm Periodic Pattern of a Singlet Concave Nanoring in the C Orientation of Nanocrescents** When a singlet concave nanoring similar to those inspected in a (i) hexagonal pattern is arranged into a 300 nm periodic rectangular pattern, in the rectified absorbance there appears a global maximum (at 590 nm) in the C orientation of horizontal singlet (slightly rotated quadrumer concave nanocrescents) ( $0^\circ$  ( $16^\circ$ ) azimuthal angle)) and is followed by a tiny shoulder at 640 nm in the  $16^\circ$  azimuthal orientation (Fig. 4a). The  $B_z$  ( $E_z$ ) distribution exhibits lobes perpendicular (parallel) to the  $\vec{E}$ -field direction at the global maximum. Accordingly, the characteristic charge distribution at the r-C resonance consists of reversed dipoles on the inner and outer rims of the nanoring along the  $\vec{E}$ -field direction. Given the spherical symmetry of the concave singlet nanorings,

this characteristic charge distribution should be insensitive to the  $\vec{E}$ -field direction. The tiny shoulder in  $16^\circ$  azimuthal orientation indicates a cross-coupling effect caused by the existing  $\vec{E}$ -field component along the  $\vec{k}_p$  vector of the pattern. However, instead of a horizontal cross-coupled r-U mode, the reversed dipoles rotate on the nanoring (Fig. 4b, top). The r-C LSPR on the singlet nanoring results in a single flat band in the dispersion characteristics (Fig. 4c, left).

**Rectangular 300 nm Periodic Pattern of a Singlet Concave Nanoring in The U Orientation of Nanocrescents** In comparison, in the rectified absorbance of the 300 nm periodic rectangular array composed of a singlet concave nanoring, the local maximum appearing at a slightly reduced wavelength of 560 nm is followed by a global maximum at 640 nm in the U orientation of horizontal singlet nanocrescent (slightly rotated quadrumer concave nanocrescents) ( $90^\circ$  ( $106^\circ$ ) azimuthal angle) (Fig. 4a). At the local maximum, the  $B_z$  ( $E_z$ ) lobes are perpendicular (parallel) to the  $\vec{E}$ -field direction. Accordingly, the characteristic charge distribution at the r-U resonance consists of reversed dipoles on the inner and outer rims of the concave singlet nanorings along the  $\vec{E}$ -field direction. In contrast, at the global maximum both for  $90^\circ$  and  $106^\circ$  azimuthal orientations, the  $B_z$  ( $E_z$ ) field lobes are completely perpendicular (parallel) to the  $\vec{k}_p$  lattice vector. As a result, the  $B_z$  ( $E_z$ ) lobes are rotated clockwise to a lesser extent compared with the local maximum in  $106^\circ$  azimuthal orientation. This indicates that the grating-coupling effect dominates with a strength correlated with the  $\vec{E}$ -field component along the  $\vec{k}_p$  direction. Accordingly, at the global maximum, the horizontal reversed dipoles and the strong periodic charge modulation along the  $\vec{k}_p$  lattice vector demonstrate the grating-coupling of SPP1 modes of the (1, 0) order, which are more (less) pronounced in the  $90^\circ$  ( $106^\circ$ ) azimuthal orientation (Figs. 4b, bottom and 4c, right). The interacting r-U LSPR on the singlet nanoring and the SPP1 on the pattern results in anticrossing bands in the dispersion characteristics (Fig. 4c, right).

#### Rectangular 300 nm Periodic Pattern of a Horizontal Singlet Concave Nanocrescent

**Rectangular 300 nm Periodic Pattern of a Horizontal Singlet Concave Nanocrescent in the C Orientation** When a

singlet horizontal concave nanocrescent is arranged into a 300 nm periodic rectangular array, only a shoulder appears in the rectified absorptance at 590 nm (580 nm) before the global maximum at 640 nm in (close to) the C orientation ( $0^\circ$  ( $16^\circ$ ) azimuthal angle) (Fig. 5a). On the  $B_z$  distribution, the four nearest-neighbor c-C2 resonance-related lobes and the two c-C1 resonance-related lobes result in four lobes at the shoulder, with maximum intensity at the nanocrescent tips. This is accompanied by two  $E_z$  lobes, with the stronger one appearing on the smaller arch of the nanocrescents. A quadrupolar and hexapolar charge distribution also appears in a noticeable fraction within one cycle of the time-dependent charge distribution. In contrast, at the global maximum, the two tips are coincident with the maxima on the  $B_z$  distribution, whereas the accompanying  $E_z$  distribution indicates two lobes on the two arches of the nanocrescents: the stronger lobe appears on the smaller arch for both  $0^\circ$  and  $16^\circ$  azimuthal orientations. Thus, on the singlet concave nanocrescent in  $0^\circ$  azimuthal orientation, the characteristic charge distribution is dipolar along the  $\vec{E}$ -field direction at the c-C1 resonance (Fig. 5b, top). The weakly interacting c-C2 and c-C1 LSPRs on the horizontal singlet nanocrescent result in two overlapping flat bands in the dispersion characteristics (Fig. 5c, left).

**Rectangular 300 nm Periodic Pattern of a Horizontal Singlet Concave Nanocrescent in the U Orientation** In comparison, for the rectified absorptance of the 300 nm periodic rectangular array composed of concave nanocrescents, a local maximum at 560 nm (570 nm) appears before the global maximum at 610 nm in (close to) the U orientation ( $90^\circ$  ( $106^\circ$ ) azimuthal angle). In addition to this, a shoulder appears at 640 nm in the  $106^\circ$  azimuthal orientation (Fig. 5a). Two  $B_z$  lobes appear on the arches of the nanocrescents at the local maximum, with the stronger lobe appearing on the larger arch. This is accompanied by four  $E_z$  lobes on the nanocrescent. Accordingly, a quadrupolar charge distribution is characteristic at the c-U resonance on the horizontal singlet concave nanocrescent (Fig. 5b, bottom). In contrast, at the global maximum two lobes appear on the  $B_z$  distribution, the lobe on the tip becomes intense to the same degree as the lobe on the larger arch (the bridge between the tips disappears), whereas the accompanying  $E_z$  distribution still has four lobes, although two of these lobes have larger intensity on the smaller arch close to the nanocrescent tips. The characteristic charge distribution is still quadrupolar. In addition to this, a strong (weak) periodic charge modulation appears, which originates from grating-coupling of the order (1, 0) SPP1 modes. This reveals that SPPs are more (less) efficiently coupled when the  $\vec{E}$ -field oscillates along (almost parallel to)  $\vec{k}_p$  in the  $90^\circ$  ( $106^\circ$ ) azimuthal orientation (Fig. 5b, bottom and 5c, right). At the shoulder, and appearing exclusively in the  $106^\circ$  azimuthal

orientation, two  $B_z$  lobes are apparent, distributed asymmetrically on the crescent tips. This is accompanied by two lobes on the  $E_z$  distribution on the nanocrescent arches, with larger intensity on the small arch. The dominant charge distribution indicates the dipolar c-C1 resonance, which is cross-coupled because of the  $\vec{E}$ -field component along the symmetry axis of the nanocrescent (Fig. 5b, bottom). The spectrum for the  $106^\circ$  azimuthal orientation is unique because the c-U resonance (at 570 nm) is followed by a peak caused by SPP1 grating-coupling at 610 nm, then a shoulder appears at 640 nm originating from the cross-coupled c-C1 resonance (Fig. 5c, right). The interacting c-U LSPR on the singlet horizontal nanocrescent and the SPP1 on the pattern result in anticrossing bands in the dispersion characteristics (Fig. 5c, right).

### Rectangular 300 nm Periodic Pattern of a Quadramer of Concave Nanocrescents

**Rectangular 300 nm Periodic Pattern of a Quadramer of Concave Nanocrescents in the C Orientation** When a 300 nm rectangular pattern is composed of four slightly rotated concave nanocrescents, a shoulder appears in the rectified absorptance at 580 nm before the global maximum at 640 nm close to (in) the C orientation ( $0^\circ$  ( $16^\circ$ ) azimuthal angle) of the quadramers (Fig. 6a). In contrast with the convex quadramer counterpart, for concave patterns no such difference exists between the extrema as observed in the presence of either one or four nanocrescents [47, 48]. The field distributions are analogous with those observable on singlet nanocrescents. Specifically, the coalescence of four c-C2 resonance-related lobes and two c-C1 resonance-related lobes causes the  $B_z$  to exhibit four lobes at the shoulder, resulting in intensity maxima on the crescent tips. This is accompanied by two  $E_z$  lobes on the nanocrescent arches, with the stronger lobe appearing on the smaller arch. The charge distribution is mainly quadrupolar (i.e., no hexapolar modulation is apparent), in contrast with the horizontal singlet-nanocrescent case. At the global maximum, two lobes on the  $B_z$  distribution show intensity maxima on the nanocrescent tips, whereas the accompanying  $E_z$  distribution reveals two lobes on the arches of the nanocrescents, with the lobe on the smaller arch being significantly stronger. The characteristic charge distribution is dipolar along the  $\vec{E}$ -field direction at the c-C1 resonance of the quadramer of four nanocrescents in the  $16^\circ$  azimuthal orientation (Fig. 6b, top). The strongly interacting c-C2 and c-C1 LSPRs on the quadramer result in two slightly separated flat bands in the dispersion characteristics (Fig. 6c, left).

**Rectangular 300 nm Periodic Pattern of a Quadramer of Concave Nanocrescents in the U Orientation** In comparison, the global maximum at 560 nm in the rectified absorptance of

the 300 nm periodic rectangular array composed of concave nanocrescents is followed by a shoulder at 640 nm close to the U orientation ( $90^\circ$  azimuthal angle), whereas only a single maximum appears at 560 nm in the U orientation ( $106^\circ$  azimuthal angle) (Fig. 6a). The most important difference with respect to the unit cell with a singlet horizontal nanocrescent is the partial (complete) disappearance of the second maximum in the  $90^\circ$  ( $106^\circ$ ) azimuthal orientation. The  $B_z$  distribution exhibits two lobes at the global maximum, with the stronger lobe on the larger arch of the nanocrescents and the weaker lobe is asymmetrically (symmetrically) aligned on the crescent tips in the  $90^\circ$  ( $106^\circ$ ) orientation. The accompanying  $E_z$  distribution has four lobes asymmetrically (symmetrically) aligned with respect to the nanocrescent axis. Accordingly, a quadrupolar charge distribution develops at the c-U resonance on the quadrumer of four nanocrescents in  $106^\circ$  azimuthal orientation (Fig. 6b, bottom). In contrast, at the shoulder appearing exclusively in the  $90^\circ$  azimuthal orientation, the  $B_z$  distribution has two lobes on the crescent tips (larger arch) that become more (less) intense, whereas the  $E_z$  distribution indicates only two lobes, with the lobe on the small arch of the nanocrescents becoming more intense. The characteristic charge distribution is dipolar and, as a result, the quadrumer of nanocrescents has a net dipole moment. Comparison with the charge distribution of the C orientation at the same spectral position reveals that a dipolar charge distribution appears, analogous with that of the c-C1 charge distribution. This is due to the  $\vec{E}$ -field component lying along the symmetry axes of the concave nanocrescents, which enables cross-coupling of the c-C1 resonance in the  $90^\circ$  azimuthal orientation (Fig. 6b, bottom). Surprisingly, no SPP1 coupling is caused by the group symmetry of the quadrumer (Fig. 6c, right). The c-U LSPR on the quadrumer of nanocrescents results in a single horizontal band in the dispersion characteristics (Fig. 6c, right).

### Rectangular 300 nm Periodic Pattern of a Complex Concave Miniarray

**Rectangular 300 nm Periodic Pattern of a Complex Concave Miniarray in the C Orientation** When a 300 nm periodic rectangular pattern is composed of a complex concave miniarray consisted of both the central nanoring and quadrumer of nanocrescents, a local maximum appears in their absorbance at 590 nm before the global maximum at 640 nm close to (in) the C orientation ( $0^\circ$  ( $16^\circ$ ) azimuthal angle) (Fig. 7a). Only a slight difference occurs between the local and global maximum of the complex miniarray and the global maximum (shoulder) and shoulder in  $16^\circ$  azimuthal orientation (global maximum) in the case of a singlet nanoring (quadrumer of four nanocrescents). At the

local maximum, the  $B_z$  distribution exhibits intense lobes on the outer rim of the nanoring perpendicular to the  $\vec{E}$ -field direction. Four significantly weaker lobes appear on the nanocrescents because of the coalescence of the four and two lobes originating from c-C2 and c-C1 resonance and, as a result, asymmetrical intensity maxima appear on the tips of the nanocrescents. This is accompanied by stronger lobes on the inner rim of the nanoring developing on the  $E_z$  distribution along the  $\vec{E}$ -field direction and two lobes developing on the arches of the nanocrescents, with the one on the smaller arch being stronger. Strong reversed dipoles arise on the inner and outer rim of the nanoring along the  $\vec{E}$ -field direction, which are enhanced, especially on the inner rim. Not only a quadrupolar charge distribution but also a hexapolar charge modulation is observable that is similar to the singlet nanocrescent but contrasts with the case of the quadrumer nanocrescent (Fig. 7b, top). In contrast, at the global maximum, the nanoring exhibits significantly weaker lobes that appear exclusively on the outer rim, whereas the two lobes localized on the nanocrescent tips show asymmetrical (symmetrical) maxima on the  $B_z$  distribution. Accordingly, the accompanying  $E_z$  distribution has weak lobes of less well-defined directivity on the nanoring, whereas two significantly stronger lobes appear on the arches of the nanocrescents, especially on the smaller arch.

A dipolar charge distribution develops along the  $\vec{E}$ -field direction on the nanocrescents and exhibits a pure c-C1 resonance on the quadrumer of nanocrescents in the  $16^\circ$  azimuthal orientation, whereas weak reversed dipoles rotate on the nanoring instead of the expected horizontal cross-coupled r-U mode. The local maximum on the miniarray originates from the r-C resonance of the nanoring, which overlaps with the interacting c-C2 and c-C1 modes of the nanocrescents on the quadrumer; the latter also results in a shoulder in their spectrum. The global maximum originates mainly from the c-C1 mode on the quadrumer of nanocrescents. At the global maximum, the cross-coupled r-U resonance on the nanoring spectrally overlaps with the c-C1 resonance on the nanocrescents. The intermittent perpendicularity of the weak rotating nanoring dipole and strong nanocrescent dipoles results in a Fano interference between the two LSPRs (Fig. 7b, top and 7c, left). The r-C resonance on the nanoring and the interacting c-C2 and c-C1 LSPRs on the quadrumer result in two separated flat bands in the dispersion characteristics (Fig. 7c, left).

**Rectangular 300 nm Periodic Pattern of a Complex Concave Miniarray in the U Orientation** In comparison, the local maximum at 560 nm in the rectified absorbance of the 300 nm periodic rectangular array composed of a complex concave miniarray the local maximum (560 nm/560 nm) is followed by a narrower global maximum at 640 nm



close to (in) the U orientation ( $90^\circ$  ( $106^\circ$ ) azimuthal angle) (Fig. 7a). The most important difference with respect to the nanorescent quadrumer is the recovery of the second maximum, which has been observed already in the case of the singlet nanoring and singlet nanorescent containing unit cells in the  $90^\circ$  azimuthal orientation. The  $B_z$  distribution exhibits strong lobes on the outer rim of the nanoring oriented perpendicularly to the  $\vec{E}$ -field direction, with two lobes on the nanorescents at the local maximum. The stronger lobe appears on the larger arch of the nanorescents, whereas the weaker lobe is asymmetrically (symmetrically) distributed on the nanorescent tips in the  $90^\circ$  ( $106^\circ$ ) azimuthal orientation. This is accompanied by the  $E_z$  distribution, indicating lobes along the  $\vec{E}$ -field direction on the inner and outer rim of the nanoring, and four lobes asymmetrically (symmetrically) aligned on the nanorescents. Accordingly, reversed dipoles arise on the inner and outer rim of the nanoring along the  $\vec{E}$ -field direction at the r-U resonance, and a quadrupolar charge distribution appears on the nanorescents at the c-U resonance (Fig. 7b, bottom). In contrast, at the global maximum the two lobes on the  $B_z$  distribution on the outer rim of the nanoring are aligned perpendicularly to  $\vec{k}_p$  for both the  $90^\circ$  and  $106^\circ$  azimuthal orientations, whereas the asymmetrically distributed lobes on the crescent tips show higher intensity than the lobe on the larger arch of the nanorescents. However, the contribution of the quadrumer nanorescents is not significant at this extremum, as shown in Fig. 7b (bottom). The accompanying  $E_z$  distribution indicates two lobes on the nanoring almost along the  $\vec{k}_p$  vector, and two asymmetrical lobes on the small arch of the nanorescents that are more intense. The characteristic charge distribution includes a reversed dipolar distribution on the inner and outer rim on the nanoring along (slightly rotated with respect to) the  $\vec{k}_p$  vector and a weak quadrupolar distribution on the nanorescents. The extended periodic charge modulation corresponds to the grating-coupled, (-1,0) order SPP1 ( $\vec{k}_p \approx \vec{k}_{spp}$ ). The miniarray local maximum originates from the sum of the coincident r-U mode of the nanoring and the c-U modes on the quadrumer of nanorescents, whereas the grating-coupled SPP1 is responsible for the narrow global maximum (Figs. 7b, bottom and 7c, right). The r-U LSPR on the nanoring overlaps with the c-U LSPRs on the quadrumer of nanorescents and couples with the SPP1 on the rectangular ring pattern, which results in anticrossing bands in the dispersion characteristics (Fig. 7c, right).

### Rectangular 600 nm Periodic Pattern of a Complex Concave Miniarray

**Rectangular 600 nm Periodic Pattern of a Complex Concave Miniarray in the C Orientation (600 nm)** When a twofold

larger 600 nm periodic rectangular pattern is composed of the same complex concave miniarray consisted of the central nanoring and quadrumer of nanorescents, a local maximum appears in their absorptance at 590 nm before the global maximum at 640 nm. Moreover, no (noticeable) modulation appears at longer wavelength (970 nm) close to (in) the C orientation ( $0^\circ$  ( $16^\circ$ ) azimuthal angle) (Fig. 8a). Similarly to the 300 nm periodic rectangular pattern, the local maximum of the complex miniarray is the same as (differs by only 10 nm from) the global maximum (shoulder), which is observable in the case of a singlet nanoring (quadrumer of nanorescents). The  $B_z$  distribution has lobes on the outer rim of the nanoring at the local maximum that are perpendicular to the  $\vec{E}$ -field direction. Four significantly weaker  $B_z$  lobes appear on the nanorescents and are caused by the coalescence of the four and two lobes originating from the c-C2 and c-C1 resonance, respectively. These show significantly (considerably) asymmetrical distribution in the  $0^\circ$  ( $16^\circ$ ) azimuthal orientation, which is noticeable mainly on the tips of the nanorescents. This is accompanied by an  $E_z$  distribution with stronger lobes on the inner rim of the nanoring along the  $\vec{E}$ -field direction, and two lobes on the nanorescents, the stronger of which appears on the smaller arch. Strong reversed dipoles arise on the inner and outer rim of the nanoring along the  $\vec{E}$ -field direction at the r-C resonance. A mainly quadrupolar charge distribution is observable, but a hexapolar modulation exists on the components of the quadrumer as well, similarly to the charge distribution at the shoulder on the singlet nanorescent in the rectangular pattern.

Similarly to the 300 nm periodic rectangular pattern, no difference appears between the global maximum of the complex miniarray and the shoulder (global maximum) observable for a singlet nanoring in  $16^\circ$  azimuthal orientation (quadrumer of nanorescents). Compared with the local maximum, the nanoring at the global maximum exhibits significantly weaker lobes on the outer rim perpendicular to the  $\vec{E}$ -field direction, whereas the two tips show asymmetrical (symmetrical) intensity maxima on the  $B_z$  distribution. The accompanying  $E_z$  distribution has two lobes, with the stronger lobe on the smaller arch of the nanorescents. The charge accumulation is almost negligible on the nanoring, whereas it is dipolar along the  $\vec{E}$ -field direction on the nanorescents at the c-C1 resonance on the quadrumer of nanorescents in the  $16^\circ$  azimuthal orientation of the miniarray (Fig. 8b, top). The miniarray response originates again from the sum of the r-C mode of the nanoring and the interacting c-C2 and c-C1 modes at the local maximum, and from the c-C1 modes on the nanorescents in the quadrumer of nanorescents at the global maximum. In addition to this, the r-U resonance on the nanoring cross-coupled in the  $16^\circ$  azimuthal orientation spectrally overlaps with the c-C1 resonance on the

nanocrescents at the global maximum, similarly to the 300 nm periodic pattern of the miniarray. The local maximum appearing at longer wavelength in the 16° azimuthal orientation is exceptional for the larger periodic rectangular pattern. Here, the  $B_z$  ( $E_z$ ) lobes aligned perpendicular (parallel) to the  $\vec{E}$ -field direction is more (less) well defined in the 0° (16°) azimuthal orientation. In addition, a periodic lateral modulation exists on the  $E_z$  distribution for 16° azimuthal angle that is significantly weaker at the same wavelength for 0° azimuthal angle (the latter is shown as a reference). The charge distribution consists of reversed dipoles on the nanoring along the  $\vec{k}_p$  vector, and dipoles on the nanocrescents are parallel to that on the outer rim of the nanoring. A lateral charge modulation with a period commensurate with the grating-coupled SPP1 wavelength also appears. The preference for 16° azimuthal orientation indicates that an  $\vec{E}$ -field component along the  $\vec{k}_p$  vector is required and proves that a propagating plasmonic rather than a scattered photonic mode is coupled. In fact, the wavelength of ( $\pm 1, 0$ ) order SPP1 that can be coupled at this spectral location is closer to 600 nm. At this Wood–Rayleigh anomaly, the  $E_z$  lobes are less well oriented along the  $\vec{E}$ -field direction on the nanoholes, since the charge-separation orientation is governed by SPP1 with a wave vector commensurate with  $\vec{k}_p$  (Figs. 8b, top and 8c, left). The r-C resonance on the nanoring and the interacting c-C2 and c-C1 LSPRs on the quadrumer result in two separated flat bands, and an additional Wood–Rayleigh anomaly-related band also appears in the dispersion characteristics (Fig. 8c, left).

**Rectangular 600 nm Periodic Patterns of a Complex Concave Miniarray in U the Orientation (600 nm)** In comparison, in the rectified absorptance of the 600 nm periodic rectangular array composed of complex concave miniarrays, the local maximum at 560 nm (570 nm) is followed by a large global maximum at 630 nm, and a huge modulation appears at 970 nm close to (in) the U orientation (90° (106°) azimuthal angle) (Fig. 8a). The recovery of the second maximum that has been observed for singlet nanorings and singlet nanocrescents containing unit cells occurs in the same way as for the 300 nm periodic pattern. At the local maximum the,  $B_z$  distribution exhibits strong lobes on the outer rim of the nanoring, oriented perpendicular to the  $\vec{E}$ -field direction with two lobes on the nanocrescents; the stronger lobe appearing on the larger arch and the weaker lobes distributed asymmetrically (symmetrically) on the tips in the 90° (106°) orientation. The accompanying  $E_z$  distribution indicates lobes along the  $\vec{E}$ -field direction on the inner and outer rim of the nanoring and four lobes asymmetrically (symmetrically) aligned on the nanocrescents in the 90° (106°) azimuthal orientation. Accordingly, reversed

dipoles develop on the inner and outer rims of the nanoring along the  $\vec{E}$ -field direction, and a quadrupolar charge distribution develops on the nanocrescents that corresponds to the r-U and c-U resonances on the constituents of the complex concave miniarray. At the global maximum, the lobes on the  $B_z$  distribution on the outer rim of the nanoring are aligned (almost) perpendicularly to  $\vec{k}_p$  in the 90° (106°) azimuthal orientation. In contrast with the 300 nm periodic pattern, intensity maxima appear on one of the tips and on the larger arch of the nanocrescents. The  $E_z$  distribution indicates two lobes on the nanoring along (slightly rotated with respect to)  $\vec{k}_p$ , and two asymmetrical lobes that show larger intensity on the small arch of the nanocrescents (even larger than those of the 300 nm periodic pattern). The contribution of quadrumer nanocrescents is not significant at this extremum, as is the case for the 300 nm periodic pattern (Figs. 7b, and 8b, bottom). In addition, a periodic modulation also appears along  $\vec{k}_p$ . The characteristic charge distribution includes a reversed dipolar distribution on the inner and outer rim along (slightly rotated with respect to)  $\vec{k}_p$  and a weak quadrupolar distribution on the nanocrescents. The periodic charge modulation corresponds to the grating-coupled, (2, 0) order SPP2, which is analogous to the (1, 0) order SPP1 coupled on the 300 nm pattern of a singlet nanoring, a singlet nanocrescent, and the same miniarray composed unit cells. However, given the two-fold larger period, the unit cell spans two periods of charge modulation. The local maximum of the miniarray originates again from the sum of the coincident r-U mode of the nanoring and the c-U mode on the quadrumer of nanocrescents, whereas SPP2 grating-coupling is responsible for the narrow global maximum (Figs. 8b, bottom and 8c, right). The large (pronounced) local maximum related to the Wood–Rayleigh anomaly appearing at longer wavelength is exceptional because, in this case, grating-coupling occurs in a spectral interval separated from the LSPR supported by components of the miniarray. Here,  $B_z$  ( $E_z$ ) lobes are aligned perpendicular (parallel) to the  $\vec{E}$ -field direction for both the 90° and 106° azimuthal orientations and, in addition, the  $E_z$  distribution undergoes a strong periodic lateral modulation. The corresponding charge distribution consists of reversed dipoles on the nanoring along  $\vec{k}_p$  and dipoles on the nanocrescents parallel to that on the outer rim of the nanoring. For both orientations, a lateral charge modulation dominates with a period equal to the wavelength of coupled ( $\pm 1, 0$ ) order SPP1 the (Figs. 8b, bottom and 8c, right). The r-U LSPR on the nanoring overlaps with the c-U LSPRs on the quadrumer of nanocrescents and couples with the SPP2 on the rectangular ring pattern, which results in anticrossing bands, and an additional Wood–Rayleigh anomaly-related band also appears in the dispersion characteristics (Fig. 7c, right).

## Enhancement of Dipolar Emitters Via Rectangular Patterns of Different Nano-Objects

When four dipoles are embedded into the concave nanorings that compose a 300 nm rectangular pattern, both radiative rate enhancement spectra computed either close to or in the C orientation exhibit a global maximum at 600 nm originating from the r-C mode. In addition, a local maximum appears at 640 nm due to cross-coupling of the r-U mode in the 16° azimuthal orientation. The global maximum is red-shifted by 10 nm compared with the counterpart extremum, whereas the local maximum is coincident with the shoulder in the plane-wave-illuminated absorptance spectrum. Close to or in the U orientation of quadrumer nanocrescents, a local maximum at 550 nm and a global maximum at 640 nm appear and correspond to the r-U resonance on the nanoring and to the grating-coupled SPP1, respectively. The local maximum is red-shifted by 10 nm, whereas the global maximum is coincident with the counterpart maximum in the plane-wave-illuminated absorptance spectra (Fig. 9a). When four dipoles are embedded into slightly rotated nanocrescents that compose a quadrumer close to or in the C orientation, a local maximum appears instead of a shoulder, which is followed by a global maximum. The local maximum corresponds to the mixed c-C2 and c-C1 modes, whereas the global maximum originates from the c-C1 resonance. The local maximum at 580 nm and the global maximum at 650 nm appear at a location coincident and red-shifted by 10 nm with respect to the counterpart extremum in the absorptance spectra of plane-wave-illuminated quadrumers, respectively. Close to (in) the U orientation, a c-U resonance-related local (global) maximum appears at 580 nm, which is red-shifted by 20 nm with respect to the counterpart global maximum in the plane-wave-illuminated absorptance spectrum. In addition to this close-to-U orientation (90° azimuthal angle), a global maximum appears at 650 nm, which originates from the cross-coupled c-C1 mode and is red-shifted by 10 nm with respect to the counterpart local maximum in the plane-wave-illuminated absorptance spectrum (Fig. 9b). For the rectangular pattern composed of a complex miniarray, the peaks in the enhancement spectra are added but almost inherit the profile of the nanoring and quadrumer spectra, which reveals that a weak interaction occurs between the constituent concave nano-objects in the miniarray, even if they are illuminated by dipoles. Specifically, local maximum appears at the 590-nm spectral location corresponding to the r-C resonance on the nanoring overlapped with the mixed c-C2 and c-C1 resonance on the quadrumer of nanocrescents, whereas a large global maximum appears at 650 nm that originates from the c-C1 resonance on the quadrumer of nanocrescents and is overlapped with the cross-coupled r-U mode on the nanoring.

The local maximum is coincident, whereas the global maximum is red-shifted by 10 nm with respect to the counterpart global maxima in the absorptance spectra of plane-wave-illuminated miniarrays, respectively. In the U orientation, the local maximum at 560 nm originates from the r-U and c-U resonances on the nanoring and nanocrescents, whereas the global maximum at 650 nm originates from the grating-coupled SPP1 modes. The former is coincident whereas the latter is red-shifted by 10 nm with respect to counterpart extremum in the absorptance spectra of plane-wave-illuminated miniarrays (Fig. 9).

## Discussion and Conclusion

The inspection of the reference hexagonal nanohole patterns uncovered the LSPRs that are also excited on rectangular nanohole patterns (Fig. 3). For rectangular patterns, the common difference between the charge and near-field distributions is the clockwise rotation in the 16° and 106° azimuthal orientation with respect to the distributions observable at 0° and 90° azimuthal angles (Figs. 4–8). For a rectangular pattern of a singlet concave nanoring mainly the clockwise rotation of the reversal dipoles is observable at the common extrema. For 16° azimuthal orientation, namely in the C orientation of quadrumers, a shoulder appears, which is caused by r-U mode cross-coupling that is in turn promoted by the horizontal  $\vec{E}$ -field component. Surprisingly, the localized charge distribution rotates in the 16° azimuthal orientation. In or close to the U orientation after the local maximum related to the r-U mode, a global maximum appears both at 90° and 106° azimuthal angles. The dominant  $\vec{E}$ -field component along  $\vec{k}_p$  results in (1, 0) order SPP1 grating-coupling accompanied by a periodic modulation both on the  $E_z$  and charge distributions. This periodic modulation is stronger for the 90° azimuthal orientation, whereas for the 106° azimuthal orientation both the  $B_z$  and  $E_z$  distributions and the charge distribution are governed by competition between the r-U LSPR and the grating-coupled SPP1 mode (Fig. 4). On the rectangular pattern of a horizontal singlet concave nanocrescent, the c-C and c-U resonance arises for 0° and 90° azimuthal orientation, which results in perfect alignment of the local fields parallel and perpendicular to the nanocrescent symmetry axes, respectively. In or close to the C orientation, quadrupolar and hexapolar charge distribution is also observable at the shoulder. However, the hexapolar modulation is less dominant in the 16° azimuthal orientation, so the  $E_z$  distribution is forward rotated with respect to the nanocrescent symmetry axis. A symmetric (asymmetric) dipolar distribution develops in the 0° (16°) azimuthal orientation at the global maximum. In (close to) the U orientation, a symmetric (asymmetric) quadrupolar distribution develops both at the local and global maxima.

A narrow global maximum appears that originates from the grating-coupling of SPP1 of the order (1, 0) both for 90° and 106° azimuthal angles. The quadrupolar LSPR is accompanied by a periodic modulation at the global maximum both on the  $E_z$  and charge distributions, which is stronger in the 90° azimuthal orientation because the  $\vec{E}$ -field is parallel to  $\vec{k}_p$ . In addition to this, a shoulder appears in the 106° azimuthal orientation that originates from a cross-coupled c-C1 resonance (Fig. 5). The C and U resonance arises for 16° and 106° azimuthal orientation on the rectangular pattern of quadrumers, which can result in perfect alignment of the local fields parallel and perpendicular to the symmetry axes of the slightly rotated nanocrescents, respectively. Consequently, close to (in) the C orientation (0° (16°) azimuthal angle) of the rectangular quadramer pattern, the charge distribution at the shoulder is asymmetrically (symmetrically) quadrupolar, whereas at the global maximum is asymmetrically (symmetrically) dipolar. Close to (in) the U orientation (90° (106°) azimuthal angle), the quadrupolar charge distribution is asymmetrical (symmetrical) on each constituent nanocrescent at the global maximum. The additional shoulder, which appears in the 90° azimuthal orientation of the quadramer, originates from a cross-coupled c-C1 resonance (Fig. 6). The 300 nm periodic rectangular pattern of a concave miniarray inherits the features of the rectangular patterns composed of the singlet nanoring and the quadramer of nanocrescents. Caused by the non-parallel alignment with respect to the  $\vec{E}$ -field direction, the modes on the nano-objects interact close to the C orientation (0° azimuthal angle) and more commensurate charge and field accumulation is observable on the nanocrescents at the local maximum and on the nanoring at the global maximum. In comparison, the parallel alignment of the fields along the symmetry axes of the nanocrescents in the C orientation (16° azimuthal angle) causes the charge and field distribution to be more dominant on the nanoring at the local maximum and on the nanocrescents at the global maximum complementary. The  $E_z$  lobes are perfectly aligned along the  $\vec{E}$ -field direction on the nanocrescents in the C orientation both at the local and global maxima, whereas the  $E_z$  lobes are parallel (of less well-defined directivity with respect) to the  $\vec{E}$ -field direction on the nanoring at the local (global) maximum. Close to the U orientation (90° azimuthal angle) the subsets of nanocrescents are more distinguishable at the local maximum. A weak asymmetrical quadrupolar distribution develops on the nanocrescents in 90° azimuthal orientation also at the global maximum, but this is accompanied by a noticeable periodic modulation both on the  $E_z$  and charge distributions because the  $\vec{E}$ -field is parallel to  $\vec{k}_p$ . In comparison, the subsets of nanocrescents are less distinguishable in the U orientation (106° azimuthal angle) at the local maximum. A weak asymmetrical quadrupolar distribution develops on the nanocrescents in the U orientation (106°

azimuthal angle) at the global maximum, which is perturbed both on the  $E_z$  and charge distributions by a relatively weaker periodic modulation due to the misalignment between the  $\vec{E}$ -field and  $\vec{k}_p$  directions. The 600 nm periodic rectangular pattern composed of a concave miniarray exhibits features similar to those of the 300 nm periodic pattern. The differences between the perfect and non-perfect orientations are slightly less well defined, which can be explained by the smaller surface fraction of the nano-objects in the unit cell. In the C orientation the  $E_z$  lobes are perfectly aligned along the  $\vec{E}$ -field direction on the nanocrescents, both at the local and global maxima, whereas on the nanoring the  $E_z$  field lobe is parallel (of less well defined directivity with respect to) to the  $\vec{E}$ -field direction at the local (global) maximum. In the spectral interval of the ( $\pm 1$ , 0) order SPP1, grating-coupling occurs outside the LSPR (Wood–Rayleigh anomaly) in the 16° azimuthal orientation, on both the  $E_z$  and the charge distribution a modulation related to the propagating modes is noticeable. However, the modulation is significantly stronger than the periodic modulation close to the C orientation (0° azimuthal angle). In the U orientation, the LSPRs on the nanocrescents are slightly less distinguishable at the local maximum; however, at the global maximum, the periodic modulation accompanying the grating-coupled (-2,0) order SPP2 is slightly weaker both on  $E_z$  and charge distributions. In addition, the grating-coupling of the ( $\pm 1$ , 0) order SPP1 modes through the  $\vec{k}_p$  lattice vector results in a Wood–Rayleigh anomaly with considerable efficiency; however, it is slightly smaller than that achieved close to the U orientation (90° azimuthal angle). The dispersion characteristics have been computed for 0° and 90° azimuthal orientations (Figs. 3d, 3e, and 4–8c). In the present systems, grating-coupling does not occur in the 0° azimuthal orientation in the inspected spectral interval because of the large  $kt$  corresponding to the small  $t$  unit cell side length. In contrast, the coupling for the 90° azimuthal orientation via the  $\vec{k}_p$  grating vector of the rectangular lattice results in well-defined bands in the inspected wavelength interval, except the 300 nm periodic pattern of the quadramer of nanocrescents. The dispersion characteristics of the hexagonal pattern of concave nanorings do not depend on azimuthal orientation (Fig. 3d). A well-defined and tilting-independent flat band is identifiable, which corresponds to the identical r-C and r-U LSPR on the nanorings in 0° and 90° azimuthal orientation, respectively. In comparison, a tilting-independent flat band corresponding to the r-C resonance is observable in the dispersion characteristics of the rectangular pattern of concave nanorings computed for 0° azimuthal orientation, whereas for 90° azimuthal orientation, the flat band corresponding to the r-U resonance is perturbed by the grating-coupled (1, 0) order SPP1 band (Fig. 4c). The dispersion characteristics of the hexagonal pattern of concave nanocrescents, 300 nm periodic rectangular pattern of a horizontal



singlet concave nanocrescent, and a quadrumer of slightly rotated concave nanocrescents, as well as the 300 nm and 600 nm rectangular pattern of the complex miniarray exhibit well-defined and similar LSPR-related bands, all depend similarly on the azimuthal orientation (Figs. 4e and 58c). For the 0° azimuthal orientation of the hexagonal pattern and of the rectangular pattern of a singlet horizontal nanocrescent and a quadrumer of slightly rotated nanocrescents, a strong tilting-independent flat band indicates the c-C1 LSPR, whereas the interaction of the c-C2 and c-C1 modes results in a ghost flat band at slightly shorter wavelength. This interaction-related band is less (more) defined for a horizontal singlet (slightly rotated quadrumer) nanocrescent in a rectangular pattern (Figs. 3e, 5, 6c, left). In the 90° azimuthal orientation of the rectangular patterns, the flat band corresponding to the c-U resonance is perturbed by the grating-coupled (-1,0) order SPP1 band in the presence of a singlet nanocrescent, whereas no grating-coupled SPP band exists in the presence of a quadrumer of nanocrescents (Figs. 3e, 5, 6c, right). The dispersion characteristics of the 300- and 600 nm periodic rectangular patterns of the miniarray are more complex. Similarly to the constituent nano-objects, in the 0° azimuthal orientation of the 300- and 600 nm periodic rectangular patterns, a tilting-independent weak flat band indicates the c-C1 LSPR on the nanocrescents, whereas the interaction of the c-C2 and c-C1 modes results in a flat band, which overlaps with the strong, tilting and azimuthal-orientation-independent band of the r-C LSPR on the nanoring (Figs. 7 and 8c, left). In addition, on the 600 nm periodic rectangular pattern, the Wood–Rayleigh-anomaly-related band is noticeable due to the grating-coupling of the ( $\pm 1, 0$ ) order SPP1 along  $\bar{k}_p$  of the periodic pattern, which results in a tiny peak also at perpendicular incidence in 16° azimuthal orientation (Figs. 7 and 8c, left). For the 90° azimuthal orientation of the 300- and 600 nm periodic patterns of the complex miniarray, the strong, tilting-independent band corresponding to the coincident r-U LSPR on the nanoring and c-U LSPR on the nanocrescents is perturbed by the (-1, 0) and (-2, 0) order SPPs, respectively. In addition, for the 600 nm periodic rectangular pattern, the SPP band related to the Wood–Rayleigh anomaly also appears because of the efficient ( $\pm 1, 0$ )-order coupling of plasmonic modes along the  $\bar{k}_p$  vector of the periodic pattern, which results in significant (considerable) peaks at perpendicular incidence in the 90° (106°) azimuthal orientation (Figs. 7 and 8c, right). The peaks corresponding to SPP coupling are distinguished from LSPRs by two important differences: (i) The periodic charge distribution (and the related  $E_z$  distribution) is parallel to  $\bar{k}_p$  rather than governed by the  $\vec{E}$ -field direction because the latter determines only the charge separation of the LSPR. (ii) The period of the modulation appearing both on the  $E_z$  and charge distributions equals to the wavelength of the (-1, 0) and (-2, 0) order grating-coupled SPP modes for 90°

azimuthal orientation of the 300- and 600 nm periodic patterns in the spectral interval overlapping with the LSPR (640 nm and 630 nm). In the absence of LSPR (970 nm), the period of the modulation reveals the relatively stronger (weaker) grating-coupling of the order ( $\pm 1, 0$ ) SPP1 in 90° (106°) and 16° azimuthal orientation for the 600 nm periodic pattern. This study proves that significant enhancement of dipolar emitters is achievable in spectral intervals of plasmonic resonances on complex concave patterns tunable by integrated lithography.

**Acknowledgements** This work was supported by the National Research, Development and Innovation Office (NKFIH) “Optimized nanoplasmonics” (K116362) and the European Union, co-financed by the European Social Fund. “Ultrafast physical processes in atoms, molecules, nanostructures and biological systems” (EFOP-3.6.2-16-2017-00005). S. Sipo gratefully acknowledges the support of NKFIH PD-121170.

**Funding** Open access funding provided by University of Szeged. This study was funded by Emberi Eroforrások Minisztériuma (EFOP-3.6.2-16-2017-00005), Dr. Maria Csete from Nemzeti Kutatási és Technológiai Hivatal (K116362), and Dr. Áron Sipo from Nemzeti Kutatási és Technológiai Hivatal (PD121170).

**Open Access** This article is licensed under a Creative Commons Attribution 4.0 International License, which permits use, sharing, adaptation, distribution and reproduction in any medium or format, as long as you give appropriate credit to the original author(s) and the source, provide a link to the Creative Commons licence, and indicate if changes were made. The images or other third party material in this article are included in the article’s Creative Commons licence, unless indicated otherwise in a credit line to the material. If material is not included in the article’s Creative Commons licence and your intended use is not permitted by statutory regulation or exceeds the permitted use, you will need to obtain permission directly from the copyright holder. To view a copy of this licence, visit <http://creativecommons.org/licenses/by/4.0/>.

## References

1. Ebbesen T, Lezec H, Ghaemi H, Thio T, Wolff PA (1998) Extraordinary optical transmission through sub-wavelength hole arrays. *Nature*. 391:667–669. <https://doi.org/10.1038/35570>
2. de Abajo FJG (2007) Colloquium: Light scattering by particle and hole arrays. *Reviews of Modern Physics*. 79:1267. <https://doi.org/10.1103/RevModPhys.79.1267>
3. Genet C, Ebbesen TW (2007) Light in tiny holes. *Nature*. 445:39–46. <https://doi.org/10.1038/nature05350>
4. Gordon R, Brolo A, Sinton D, Kavanagh K (2010) Resonant optical transmission through hole-arrays in metal films: physics and applications. *Laser & Photonics Reviews*. 4:311–335. <https://doi.org/10.1002/lpor.200810079>
5. Garcia-Vidal FJ, Martin-Moreno FJ, Ebbesen TW, Kuipers L (2010) Light passing through sub-wavelength apertures. *Reviews of Modern Physics*. 82:729–787. <https://doi.org/10.1103/RevModPhys.82.729>
6. Shi X, Hesselink L, Thornton RL (2003) Ultrahigh light transmission through a C-shaped nanoaperture. *Optics Letters*. 28:1320–1322. <https://doi.org/10.1364/OL.28.001320>

7. Ghaemi HF, Tineke T, Grupp DE, Ebbesen TW, Lezec HJ (1998) Surface plasmons enhance optical transmission through subwavelength holes. *Physical Review B*. 58:6779–6782. <https://doi.org/10.1103/PhysRevB.58.6779>
8. Barnes WL, Murray WA, Dintinger J, Devaux E, Ebbesen TW (2004) Surface Plasmon Polaritons and Their Role in the Enhanced Transmission of Light through Periodic Arrays of Subwavelength Holes in a Metal Film. *Physical Review Letters*. 92:107401. <https://doi.org/10.1103/PhysRevLett.92.107401>
9. Kelf TA, Sugawara Y, Baumberg JJ, Abdelsalam M, Bartlett PN (2005) Plasmonic band gaps and trapped plasmons on nanostructured metal surfaces. *Physical Review Letters*. 95:116802. <https://doi.org/10.1103/PhysRevLett.95.116802>
10. Zhou W, Gao H, Odom TW (2010) Toward broadband plasmonics: Tuning dispersion in rhombic plasmonic crystals. *ACS Nano*. 4:1242–1247. <https://doi.org/10.1021/nn901590p>
11. Kwak E-S, Henzie J, Chang S-H, Gray SK, Schatz GC, Odom TW (2005) Surface plasmon standing waves in large-area subwavelength hole arrays. *Nano Letters*. 5:1963–1967. <https://doi.org/10.1021/nl051339s>
12. Lee MH, Gao H, Henzie J, Odom TW (2007) Microscale arrays of nanoscale holes. *Small*. 3:2029–2033. <https://doi.org/10.1002/sml.200700499>
13. Parsons J, Hendry E, Burrows CP, Auguie B, Sambles JR, Barnes WL (2009) Localized surface-plasmon resonances in periodic nondiffracting metallic nanoparticle and nanohole arrays. *Physical Review B*. 79:073412. <https://doi.org/10.1103/PhysRevB.79.073412>
14. Yanik AA, Cetin AE, Huang M, Artar A, Mousavi SH, Khanikaev A, Connor JH, Shvets G, Altug H (2011) Seeing protein monolayers with naked eye through plasmonic Fano resonances. *Proceedings of the National Academy of Sciences of the United States of America*. 108:11784–11789. <https://doi.org/10.1073/pnas.1101910108>
15. Altewischer E, van Exter MP, Woerdman JP (2003) Polarization analysis of propagating surface plasmons in a subwavelength hole array. *Journal of the Optical Society of America B*. 20:1927–1931. <https://doi.org/10.1364/JOSAB.20.001927>
16. Masson J-B, Guilhem G (2006) Coupling between surface plasmons in subwavelength hole arrays. *Physical Review B*. 73:121401. <https://doi.org/10.1103/PhysRevB.73.121401>
17. Zhang S, Fan W, Panoiu NC, Malloy KJ, Osgood RM, Brueck SRJ (2005) Experimental Demonstration of Near-Infrared Negative-Index Metamaterials. *Physical Review Letters* 95:137404. <https://doi.org/10.1103/PhysRevLett.95.137404>
18. Tang L, Miller DA, Okyay AK, Matteo JA, Yuen Y, Saraswat KC, Hesselink L (2006) C-shaped nanoaperture-enhanced germanium photodetector. *Optics Letters*. 31:1519–1521. <https://doi.org/10.1364/OL.31.001519>
19. Coyle S, Netti MC, Baumberg JJ, Ghanem MA, Birkin PR, Bartlett PN, Whittaker DM (2001) Confined Plasmons in Metallic Nanocavities. *Physical Review Letters*. 87:176801. <https://doi.org/10.1103/PhysRevLett.87.176801>
20. Junesch J, Sannomiya T, Dahlin AB (2010) Optical properties of nanohole arrays in metal-dielectric double films prepared by mask-on-metal colloidal lithography. *ACS Nano* 6:10405–10415. <https://doi.org/10.1021/nn304662e>
21. Sannomiya T, Scholder O, Jefimovs K, Hafner C, Dahlin AB (2011) Investigation of Plasmon Resonances in Metal Films with Nanohole Arrays for Biosensing Applications. *Small*. 7:1653–1663. <https://doi.org/10.1002/sml.201002228>
22. Patoka P, Skeren T, Hilgendorff M, Zhi L, Paudel T, Kempa K, Giersig M (2011) Transmission of Light through Magnetic Nanocavities. *Small*. 7:3096–3100. <https://doi.org/10.1002/sml.201100997>
23. Gordon R, Sinton D, Kavanagh KL, Brolo AG (2008) A New Generation of Sensors Based on Extraordinary Optical Transmission. *Accounts of Chemical Research*. 41:1049–1057. <https://doi.org/10.1021/ar800074d>
24. Lesuffleur A, Im H, Lindquist NC, Oh S-H (2007) Periodic nanohole arrays with shape-enhanced plasmon resonance as real-time biosensors. *Applied Physics Letters*. 90:243110. <https://doi.org/10.1063/1.2747668>
25. H. Wei, U. Hakanson, Z. Yang, F. Hook, H. Xu: Small 4/9 (2008) 1296 Wei, H., Hakanson, U., Yang, Z., Hook, F., Xu, H.: Individual Nanometer Hole-Particle Pairs for Surface-Enhanced Raman Scattering. *Small*. 4, 1296-1300 (2008) <https://doi.org/10.1002/sml.200701135>
26. Rigneult H, Capoulade J, Dintinger J, Wenger J, Bonod N, Popov E (2005) Enhancement of Single-Molecule Fluorescence Detection in Subwavelength Apertures. *Physics Review Letters*. 95:117401. <https://doi.org/10.1103/PhysRevLett.95.117401>
27. Wenger, J., Gerard, D., Dintinger, J., Mahboub, O., Bonod, N., Popov, E., Ebbesen, T., Rigneault, H.: Emission and excitation contributions to enhanced single molecule fluorescence by gold nanometric apertures. *Optics Express* 16, 3008-3020 (2008). 10.1364/OE.16.003008
28. Langguth L, Punj D, Wenger J, Koendernik F (2013) Plasmonic Band Structure Controls Single-Molecule Fluorescence. *ACS Nano*. 7:8840–8848. <https://doi.org/10.1021/nn4033008>
29. Schwartz T, Hutchison JA, Genet C, Ebbesen TW (2011) Reversible Switching of Ultrastrong Light-Molecule Coupling. *Physical Review Letters* 106:196405. <https://doi.org/10.1103/PhysRevLett.106.196405>
30. Dorofeenko AV, Zyablovsky AA, Vinogradov AP, Andrianov ES, Pukhov AA, Lisyansky AA (2013) Steady state superradiance of a 2D-spaser array. *Optics Express*. 21:14539–14547. <https://doi.org/10.1364/OE.21.014539>
31. van Beijnum F, van Veldhoven PJ, Geluk EJ, de Dood MJ, Gert W, van Exter MP (2013) Surface Plasmon Lasing Observed in Metal Hole Arrays. *Physical Review Letters* 110:206802. <https://doi.org/10.1103/PhysRevLett.110.206802>
32. Van Exter M, Tenner V, van Beijnum F, de Dood M, van Veldhoven P, Geluk E (2013) Surface Plasmon Dispersion in Metal Hole Array Lasers. *Optics Express* 21:7422–7437. <https://doi.org/10.1364/OE.21.027422>
33. Falcone, F., Lopetegi, T., Laso, M. A. G., Baena, J. D., Bonache, J., Beruete, M., Marque's, R., Martin, F., Sorolla, M.: Babinet Principle Applied to the Design of Metasurfaces and Metamaterials. *Physical Review Letters* 93, 197401 (2004). <https://doi.org/10.1103/PhysRevLett.93.197401>
34. Wang Y, Yang J-K (2019) Directional coupling of surface plasmon polaritons at complementary split-ring resonators. *Scientific Reports* 9:7348. <https://doi.org/10.1038/s41598-019-43914-z>
35. Y. Chen, X. Yang J. Gao: Spin-Selective Second-Harmonic Vortex Beam Generation with Babinet-Inverted Plasmonic Metasurfaces. *Advanced Optical Materials* 1800646 (2018). <https://doi.org/10.1002/adom.201800646>
36. Horak M, Krapek V, Hrton M, Konecna A, Ligmajer F, Stoger-Pollach M, Samoril T, Patak A, Edes Z, Metelka O, Babocky J, Sikola T (2019) Limits of Babinet's principle for solid and hollow plasmonic antennas. *Scientific Reports* 9:4004. <https://doi.org/10.1038/s41598-019-40500-1>
37. Semnani, B., Flannely, J., Maruf, R. A., Bajcsy, M.: Spin-preserving chiral photonic crystal mirror. *Light: Science & Applications* 9, 23 (2020). <https://doi.org/10.1038/s41377-020-0256-5>
38. McCord MA, Rocks MJ (1997) *Handbook of Microlithography, Micromachining and Microfabrication*, 139–249. SPIE and The Institution of Electrical Engineers, Bellingham, WA

39. Skriniarova J, Pudis D, Martincek I, Kovac J, Tarjani T, Vesely M, Turek I (2007) Periodic structures prepared by two-beam interference method. *Microelectronics Journal* 746: <https://doi.org/10.1016/j.mejo.2007.04.004>
40. Fournier-Bidoz S, Kitaev V, Routkevitch D, Manners I, Ozin GA (2004) Highly Ordered Nanosphere Imprinted Nanochannel Alumina (NINA). *Advanced Materials* 16:2193. <https://doi.org/10.1002/adma.200400484>
41. Wang, Z. B., Joseph, N., Li, L., Luk'yanchuk, B. S.: A review of optical near-fields in particle/tip-assisted laser nanofabrication. *Proc. IMechE Vol. 224 Part C: J. Mechanical Engineering Science* (2009), <https://doi.org/10.1243/09544062JMES1766>
42. Guo, W., Wang, Z. B., Li, L., Whitehead, D. J., Luk'yanchuk, B. S., Liu, Z.: Near-field laser parallel nanofabrication of arbitrary-shaped patterns. *Appl. Phys. Lett.*, 90, 243101 (2007). <https://doi.org/10.1063/1.2748035>
43. Kretzshmar I, Song JH (2011) Surface-anisotropic spherical colloids in geometric and field confinement. *Current Opinion in Colloid and Interface Science* 16:84. <https://doi.org/10.1016/j.cocis.2011.01.002>
44. Edwards TD, Yang Y, Everett WN, Bevan MA (2015) Reconfigurable multi-scale colloidal assembly on excluded volume patterns. *Scientific Reports* 5:13612. <https://doi.org/10.1038/srep13612>
45. Sipos A, Somogyi A, Szabo G, Csete M (2014) Plasmonic Spectral Engineering via Interferometric Illumination of Colloid Sphere Monolayers. *Plasmonics*. 9:1207–1219. <https://doi.org/10.1007/s11468-014-9732-1>
46. Sipos A, Toth E, Torok A, Fekete O, Szabo G, Csete M (2019) Spectral engineering via complex patterns of rounded concave and convex nanoresonators achievable via integrated lithography realized by circularly polarized light. *TechConnect Briefs*. 373–376:
47. Sipos, A., Toth, E., Fekete, O., Csete, M.: Spectral engineering via complex patterns of circular nano-object miniarrays: I. convex patterns tunable by integrated lithography realized by circularly polarized light, to be published
48. Fekete, O., Toth, E., Sipos, A., Csete, M.: Comparative study on arrays of rounded convex and concave objects achievable in integrated lithography realized by circularly polarized light, to be published
49. Born M, Wolf E (1986) *Principles of optics*. Pergamon Press, Oxford
50. Palik ED (ed) (1998) *Handbook of optical constants of solids*. Press, San Diego, Calif, Acad
51. Rochholz H, Bocchio N, Kreiter M (2007) Tuning resonances on crescent-shaped noble metal nanoparticles. *New Journal of Physics*. 9:53. <https://doi.org/10.1088/1367-2630/9/3/053>
52. Kats MA, Yu N, Genevet P, Gaburro Z, Capasso F (2011) Effect of radiation damping on the spectral response of plasmonic components. *Optics Express*. 19:21748–21753. <https://doi.org/10.1364/OE.19.021748>

**Publisher's Note** Springer Nature remains neutral with regard to jurisdictional claims in published maps and institutional affiliations.